Dynamics of the bacterial replisome

Monachino, Enrico

CHAPTER 6

A PRIMASE-INDUCED CONFORMATIONAL SWITCH CONTROLS THE INTEGRITY OF THE BACTERIAL REPLISOME

Abstract

New experimental approaches that enable access to the dynamic behaviour of multi-protein complexes have led to a picture of the *Escherichia coli* DNA-replication machinery as an entity that freely exchanges DNA polymerases and displays intermittent coupling between the helicase and DNA polymerase. Challenging the textbook model of the polymerase acting as a stable complex coordinating the replisome, these observations suggest a role of the helicase as the central hub within the replisome. We report here the molecular nature of the mechanisms that convey this newly-found plasticity to the replisome. We find that the strength of the interaction between the clamp loader of the polymerase holoenzyme and the replicative helicase increases by more than two orders of magnitude upon association of the primase with the replisome. By combining *in vitro* ensemble-averaging and single-molecule assays, we show that this conformational switch operates during replication and promotes recruitment of multiple holoenzymes at the fork. Our observations provide a molecular mechanism for polymerase exchange and offer a revised model for replication that emphasizes the stochastic nature of the DNA-replication reaction.

Enrico Monachino*, Slobodan Jergic*, Jacob S. Lewis, Zhi-Qiang Xu, Allen T.Y. Lo, Valerie L. O'Shea, James M. Berger, Nicholas E. Dixon, Antoine M. van Oijen

Manuscript to be submitted

**these authors contributed equally. E. Monachino contributed to design, perform and analyse all experiments.*

The authors would like to thank Dr. Karl E. Duderstadt and Dr. Christiaan M. Punter for ImageJ plugins, Dr. Yao Wang for purified proteins, and Dr. Harshad Ghodke for fruitful discussions.

6.1 Introduction

The *Escherichia coli* replisome is comprised of at least 12 individual proteins that work together in concert to coordinate leading- and lagging-strand synthesis during duplication of chromosomal DNA (Lewis et al., 2016) (***Figure 6.1A***). Following unwinding of the parental double-stranded (ds) DNA by the DnaB helicase, the DNA polymerase III holoenzyme (Pol III HE) synthesises DNA on the two daughter strands. The single-stranded (ss) leading strand is displaced by the helicase and duplicated continuously, while the lagging strand is extruded through the DnaB central channel, coated by ssDNA-binding protein (SSB), and converted to dsDNA discontinuously by the production of 1,000–2,000 nt Okazaki fragments (OFs) (Kornberg and Baker, 1991). The distinct asymmetry in mechanism of synthesis of the two strands finds its origin in their opposite polarity, requiring the lagging-strand synthesis to take place in a direction opposite to that of the leading-strand synthesis and unwinding. This situation is proposed to result in the formation of a lagging-strand loop (Sinha et al., 1980).

Each OF is initiated at a short RNA primer deposited by the DnaG primase for utilisation by Pol III HE. The primase requires interaction with the helicase to stimulate its RNA polymerase activity (Johnson et al., 2000). The DnaB–DnaG contact is established through the interaction between the C-terminal domain of primase, termed DnaGC (Oakley et al., 2005; Tougu and Marians, 1996), and the N-terminal domains of the helicase (Lo et al., unpublished). In *E. coli*, this interaction is weak and transient [K_D in the low μM range with fast on/off kinetics (Oakley et al., 2005)] but in *Geobacillus stearothermophillus*, they form a stable complex that can be isolated by gel filtration (Bird et al., 2000) and crystallised (Bailey et al., 2007).

In bacteria, the helicase is a homo-hexamer with a distinct two-layered ring structure. Its C-terminal ATPase RecA-like domains that power DNA unwinding have pseudo-six-fold symmetry. In contrast, the N-terminal domains display a three-fold (C3) symmetry established from a trimer of dimers that encircle the widely open (dilated) central channel that fits dsDNA [***Figure 6.1B***, left panel; (Biswas and Tsodikov, 2008; Bujalowski et al., 1994; San Martin et al., 1995; Yu et al., 1996)]. Nevertheless, the recent crystal structure of *Aquifex aeolicus* DnaB in the presence of nucleotides showed a different C3 arrangement in the N-terminal collar whereby the central pore is narrow (constricted) and large enough to accommodate only ssDNA [***Figure 6.1B***, right panel; (Strycharska et al., 2013)]. These two strikingly different structures suggest a picture with a relatively low energy barrier between the dilated and constricted states and the helicase transitioning between them as it translocates on ssDNA.

Interacting with the helicase is the Pol III HE, the complex responsible for the extension of deposited RNA primers and most of chromosomal DNA synthesis. It is composed of three functionally distinct subassemblies that can be isolated separately from individual subunits: the Pol III core (or just Pol III), the sliding clamp and the clamp loader complex (CLC) (Kelman and O'Donnell, 1995). The catalytic Pol III cores are heterotrimers of

α, ε and θ subunits (αεθ) responsible for DNA synthesis and proofreading (Maki and Kornberg, 1985; Scheuermann and Echols, 1984; Studwell-Vaughan and O'Donnell, 1993; Taft-Benz and Schaaper, 2004). The sliding clamp is a toroid-shaped homodimer of β subunits (β_2) (Kong et al., 1992). Once loaded on the DNA by the ATP-dependent activity of the CLC, it stabilises Pol III on the DNA template and improves processivity through a pair of weak interactions with the α and ε subunits (Dohrmann and McHenry, 2005; Fernandez-Leiro et al., 2015; Jergic et al., 2013; Naktinis et al., 1996). The CLC complex contains seven proteins and has the composition $\chi\psi\tau_n\gamma_{(3-n)}\delta\delta'$ [n = 0–3, where physiologically relevant assemblies are thought to have n = 2 or 3 τ subunits (Lewis et al., 2016; Reyes-Lamothe et al., 2010)]. The unique copies of δ and δ' interact with the three copies of the *dnaX* gene product oligomer [τ and/or γ; (Kodaira et al., 1983; Mullin et al., 1983)] to assemble a stable ATPase-proficient circular pentamer (Bullard et al., 2002; Jeruzalmi et al., 2001; Simonetta et al., 2009). Whereas τ is a full-length product of *dnaX*, γ is a C-terminally truncated version produced as a result of a programmed ribosomal frame-shift during translation of mRNA (Blinkowa and Walker, 1990; Flower and McHenry, 1990; Tsuchihashi and Kornberg, 1990). The accessory subunits χ and ψ form a strong heterodimeric complex that interacts with all three τ/γ subunits of the pentamer via the flexible N-terminal residues in ψ (Gulbis et al., 2004; Simonetta et al., 2009) to assemble the full CLC.

The τ subunit provides the physical connectivity between the polymerase and helicase activities. It has a five-domain structure (Gao and McHenry, 2001b), with the N-terminal domains I–III being identical to γ and responsible for ATPase-dependent clamp loading activity and oligomerisation. The C-terminal fragment that distinguishes τ from γ is termed τ_{C24}. It contains domains IV, involved in interaction with the DnaB helicase (Gao and McHenry, 2001a), and domain V, responsible for strong interaction with α that is slow to dissociate (Gao and McHenry, 2001b; Jergic et al., 2007). Consequently, the τ subunit of the CLC plays a key linking role in the replisome: it ensures cohesion of the Pol III–CLC particle $(\alpha\varepsilon\theta)_n$–$\chi\psi\tau_n\gamma_{3-n}\delta\delta'$ (n = 2–3), termed Pol III*, and links the complex to the replicative helicase (***Figure 6.1A***).

Recent advances in the field have challenged the deterministic view of the replisome as a perfectly orchestrated machine, whereby the single Pol III*, stably bound to the replication fork, replicates DNA in a strictly ordered sequence of events (Monachino et al., 2017; van Oijen and Dixon, 2015). Instead, a frequent turnover of the Pol III* in the replisome is observed (Beattie et al., 2017; Lewis et al., 2017; Q. Yuan et al., 2016), suggesting that the helicase, as opposed to the polymerase, acts as the central organising structure of the replisome. An explanation for this surprising level of plasticity can be found in the network of weak interactions that enable polymerases from solution to eventually replace polymerases at the fork (Geertsema and van Oijen, 2013; Lewis et al., 2017). However, this explanation seems at odds with reports of strong and stable interaction between multimeric τ and DnaB (Gao and McHenry, 2001a; Kim et al., 1996; Park et al., 2010; Pritchard et al., 2000).

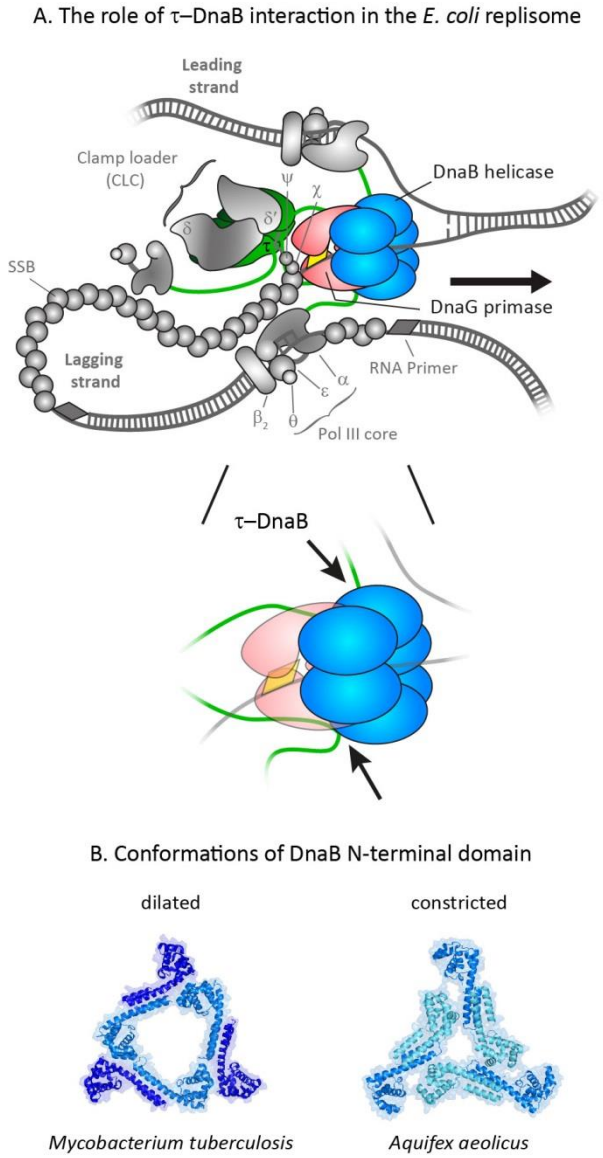

Figure 6.1: DnaB and its binding partners in the *Escherichia coli* replisome
(A) Schematic representation of the *E. coli* replisome (top panel). The focus of this study is on the DnaB helicase, as the central hub during DNA replication, and its interactions with the DnaG primase and the Pol III HE through the CLC τ subunit. DnaB, DnaG, and τ are presented in colours and reiterated for clarity in the enlarged cartoon, bottom panel. The other components of the elongating replisome (αεθ Pol III cores, β_2 sliding clamps, SSB, and CLC subcomplexes δδ' and χψ) are shown in shades of grey. (B) The two extreme conformations of DnaB helicase N-terminal domains: dilated (left panel) and constricted (right panel) conformations, as obtained from the crystal

structures of DnaB (domains) from *Mycobacterium tuberculosis* and *Aquifex aeolicus*, respectively.

We present here an unexpected conformational switch in the helicase that is triggered upon binding of DnaGC, the DnaB-interacting domain of the DnaG primase, which increases the strength of the DnaB–CLC interaction by more than two orders of magnitude. We find that in solution, DnaB is almost exclusively in the constricted state, exactly as observed in the crystal structure of *Aquifex aeolicus* DnaB. However, during replication, it transitions between the dilated and constricted states in a manner that is controlled by the primase concentration and priming K_M. We further show that the DnaB is an active helicase in both states. Finally, we use single-molecule visualisation of Pol III during replication to show that the primase concentration modulates both the kinetics of polymerase exchange in and out of the replisome and the steady-state number of polymerases associated with the replication fork. Taken together, our observations point to a model in which interaction of the primase with the helicase acts as a switch to control the organization and dynamics of the replisome, with implications for the coordination of leading- and lagging-strand synthesis, coupling between polymerase and helicase, and timing of Okazaki-fragment synthesis.

6.2 Results

6.2.1 χψ as molecular anchor for the clamp-loader complex in surface-plasmon resonance (SPR) assays

Due to its weak nature as well as complex stoichiometry, the interaction between multiple τ subunits in the CLC and DnaB is poorly understood. Previous studies employed SPR to identify the region within τ that is responsible for binding to DnaB (Gao and McHenry, 2001a), but the use of monomeric τ fragments immobilised on the surface makes it challenging to interpret these results in the context of multiple τ subunits within the CLC interacting with DnaB simultaneously. To study these interactions in a context that closely represents the physiologically relevant system, we aimed to immobilise the entire CLC onto a streptavidin (SA)-coated chip surface through an N-terminally biotinylated χ subunit, and use this surface-immobilised CLC as a platform to measure interactions with the helicase.

The stability of the CLC on the SA chip was first assessed by monitoring the dissociation of bio-τ_3CLC assembled *in situ* from immobilised bio-χψ and associated $\tau_3\delta\delta'$ (***Figures 6.S1A–S1C***). In a high ionic strength buffer (200 mM NaCl), the dissociation was moderately slow (a dissociation half-life $t_{1/2}$ of ~50 min) and was unaffected by the presence of 1 mM ADP in the buffer (***Figure 6.S1C***). In addition, the dissociation of ψ from immobilised χ was slow (***Figure 6.S1B***) and re-injection of the same concentration of $\tau_3\delta\delta'$ (100 nM) after ~2 days led to 50% of the original signal recovery (not shown) indicating that

the population of ψ still bound to bio-χ was halved, thus suggesting a $t_{1/2}$ for the χ–ψ interaction of ~2 days. Short injection of 1 M $MgCl_2$ resulted in loss of ~25% of mass from the surface (***Figure 6.S1D***) and initiated faster dissociation ($t_{1/2}$ ~ 10 min), which could be slowed down to the original level only if both δ and δ' were injected over the surface ($t_{1/2}$ ~ 45 min; ***Figure 6.S1E***), but not δ' alone (***Figure 6.S1F***). We did not inject δ alone because δ interacts weakly with τ/γ in the absence of δ' (Onrust et al., 1995a). The data indicated that the treatment with 1 M $MgCl_2$ could not regenerate the bio-χψ surface, but rather led to separation of δδ', followed by ~five-fold faster dissociation of τ_3 from ψ (Simonetta et al., 2009). Considering that δδ' does not contact ψ directly (Glover and McHenry, 1998; Simonetta et al., 2009), the change in dissociation rate revealed the contribution of δδ' to the proper conformation of τ_3 in a circular pentameric core of the CLC for the interaction with ψ. Taken together, our data are consistent with the observation of a wholesale dissociation of the entire τ_3δδ' from χψ in SPR buffer with 200 mM NaCl, thus pointing towards the ψ–$(\tau/\gamma)_3$ interaction as the weakest link in bio-CLC.

It was of importance to determine the stability of CLC on the chip surface in order to improve it for further studies. Since we determined that the stability of CLC is directly related to the slow dissociation of τ_3 from ψ and considering that a bio-χψ surface could not be efficiently regenerated, we set out to investigate the kinetics of χψ–γ_3δδ'/$\tau_2\gamma$δδ' interactions using single-shot kinetics on the multiplexed ProteOn SPR system. Previous SPR measurements indicated that the K_D for the χψ–τ/γ interaction is ~2 nM at relatively low ionic strength (100 mM K-Glu) (Olson et al., 1995). Our analysis indicated that the ψ–$(\tau/\gamma)_3$ interaction should be stronger if $(\tau/\gamma)_3$ is part of a circular pentamer. We measured the binding kinetics parameters for χψ–γ_3δδ'/$\tau_2\gamma_1$δδ' interactions by injecting various concentrations of CLC cores over immobilised bio-χψ in a buffer containing 200 mM NaCl. Irrespective of the CLC core used, we measured a dissociation half-life of ~50 min (***Table 6.1***; ***Figures 6.S2A and 6.S2B***, top panels), and dissociation constants of ~1 and ~2 nM for χψ–γ_3δδ' and χψ–$\tau_2\gamma_1$δδ', respectively.

Interaction	K_D (nM)	k_a ($M^{-1}s^{-1}$)	k_d (s^{-1})	$t_{1/2}$ (min)
bio-χψ–γ_3δδ' (ATP^-)	1.1 ± 0.0	(2.06 ± 0.00)·10^5	(2.19 ± 0.00)·10^{-4}	53
bio-χψ–$\tau_2\gamma_1$δδ' (ATP^-)	2.2 ± 0.0	(9.59 ± 0.01)·10^4	(2.10 ± 0.00)·10^{-4}	55
bio-χψ–γ_3δδ' (ATP^+)	0.3 ± 0.0	(2.67 ± 0.00)·10^5	(8.10 ± 0.01)·10^{-5}	143
bio-χψ–$\tau_2\gamma_1$δδ' (ATP^+)	0.3 ± 0.0	(1.71 ± 0.00)·10^5	(5.40 ± 0.01)·10^{-5}	214

Table 6.1: Binding parameters for the bio-χψ–γ_3δδ' and bio-χψ–$\tau_2\gamma_1$δδ' interactions, with or without ATP

Equilibrium constant (K_D), and association (k_a) and dissociation (k_d) rate constants, including the calculated dissociation half time ($t_{1/2}$), were determined by simultaneous fit of sensorgrams in ***Figure 6.S2*** to a 1:1 (Langmuir) binding model. Errors are standard errors of the fit.

Searching for a further increase of CLC stability on the chip surface, we investigated the effect of adding nucleotides. ADP showed no effect during dissociation of bio-CLC (***Figure 6.S1C***). However, the ψ subunit is known to stabilise the ATP-induced conformational state of CLC (Anderson et al., 2007; Simonetta et al., 2009). Therefore ATP could be expected to stabilize the construct and in particular the ψ–(τ/γ)$_3$ link according to the principle of microscopic reversibility. Indeed, we found this to be true: 1 mM ATP increased the affinity of $\gamma_3\delta\delta'/\tau_2\gamma_1\delta\delta'$ for bio-χψ 3.5- and seven-fold (to ~0.3 nM) and increased the dissociation half-life three- and four-fold, respectively (***Table 6.1***; ***Figures 6.S2A and 6.S2B***). By reducing the buffer ionic strength to 50 mM NaCl and by chromatographic isolation of the entire bio-CLCs prior to immobilisation (***Figure 6.S3A***), we further improved the stability of CLC on the SA surface. A dissociation lifetime of >10 hours (***Figure 6.S3B***) provides us with an ideal platform to study interactions between the CLC and DnaB.

6.2.2 Clamp loader–helicase affinity increases >400-fold upon DnaGC binding

We next used SPR to test the strength of interaction between wild-type DnaB (DnaB^{wt}) and surface-immobilised bio-τ_3CLC (***Figures 6.2A and 6.2B***). Sensorgrams recorded at a range of concentrations of DnaB^{wt} injected over bio-$\chi\psi\tau_3\delta\delta'$ in a buffer containing 1 mM ADP revealed unexpectedly fast kinetics, with fast on and off rates (***Figure 6.2B***). Responses measured at equilibrium were fit to a 1:1 steady-state affinity (SSA; ***Equation 6.1***) model to yield a value of K_D of 1.3 ± 0.2 μM. Similar measurements revealed an almost identical strength and similarly fast kinetics of the bio-$\chi\psi\tau_1\gamma_2\delta\delta'$–DnaB interaction ($K_D$ = 4.1 ± 0.3 μM; ***Figure 6.S3C***). Thus, unlike the expectation based on previously published results (Gao and McHenry, 2001a; Kim et al., 1996), our data show that the interaction between CLC and DnaB^{wt} is weak and transient in nature and does not depend on the number of τ subunits.

Recent studies proposed that the τ subunit is able to differentiate between dilated and constricted DnaB states (Strycharska et al., 2013). This conclusion was based on DNA-unwinding assays performed with two mutant versions of the helicase that are stabilized in either the dilated (DnaB^{dilated}) or constricted (DnaB^{constr}) states (***Figure 6.1B***). We tested both of them for their interaction with surface-immobilised τ_3CLC using SPR. While DnaB^{constr} exhibited binding kinetics and strengths similar to that of DnaB^{wt} (K_D = 3.3 ± 0.3 μM; ***Figure 6.2C***), an injection of 250 nM DnaB^{dilated} resulted in a markedly slower dissociation from bio-$\chi\psi\tau_3\delta\delta'$ (***Figure 6.2D***). The interaction was stabilized to a level that prevented us from reliably quantifying its strength, with the dissociation of DnaB^{dilated} from bio-$\chi\psi\tau_3\delta\delta'$ now competing with the dissociation of $\tau_3\delta\delta'$ from bio-χψ. Nevertheless, the similarity of the kinetics of DnaB^{wt} and DnaB^{constr} interacting with τ_3CLC and the stark difference between those of DnaB^{wt} and DnaB^{dilated} suggest that *E. coli* DnaB^{wt} is almost entirely in the constricted state in solution.

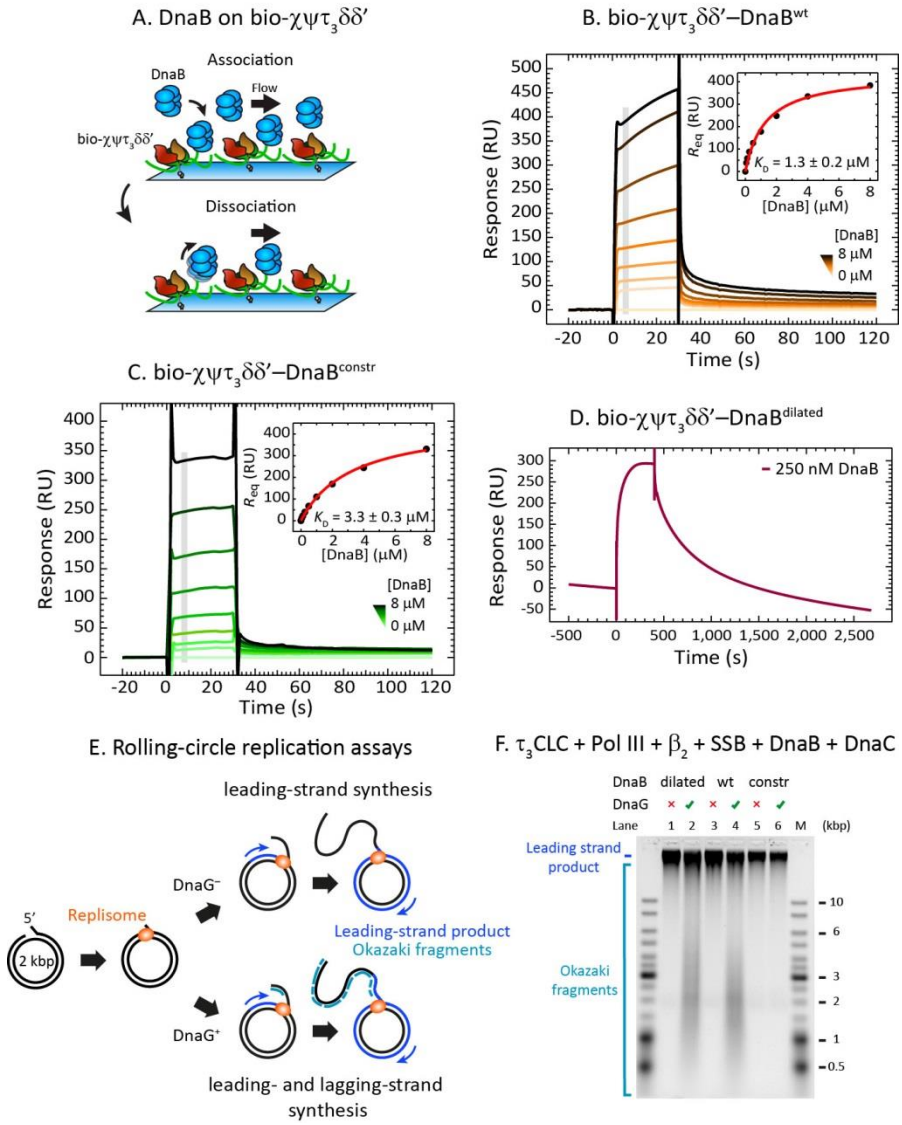

Figure 6.2: The dilated DnaB interacts strongly with bio-χψτ3δδ'

(A) Cartoon presentation of the association and dissociation phases of an SPR experiment used to measure the binding of DnaB versions in solution to immobilised bio-τ_3CLC. (B) and (C) SPR sensorgrams show association (for 30 s) and dissociation phases of bio-χψτ3δδ′–DnaB^{wt} (B) and bio-χψτ3δδ′–DnaB^{constr} (C) interactions obtained at optimised 0.0625–8 μM range of serially diluted DnaB^{wt} (B) or DnaB^{constr} (C) samples, including zero. Responses at equilibrium, determined by averaging values in the grey bar region, were fit (inset, red curve) using a 1:1 steady state affinity (SSA) model to derive dissociation constant K_D and response at saturation R_{max} values: K_D(bio-χψτ3δδ′–DnaB^{wt}) = 1.3 ± 0.2 μM and R_{max} = 440 ± 20 RU (B), and K_D(bio-

$\chi\psi\tau_3\delta\delta'$–DnaB^{constr}) = 3.3 ± 0.2 μM and R_{max} = 460 ± 20 RU (C). Errors are standard errors of the fit. (D) 250 nM DnaB^{dilated} is injected for 400 s and its slow dissociation monitored for over 2,000 s. (E) Cartoon representation of bulk replication assays with rolling-circle substrates in the absence or presence of DnaG primase, as shown in (F). The presence of DnaG enables also the lagging-strand synthesis. (F) Alkaline agarose gel showing the resolved leading strand (all lanes) and lagging strand (DnaG$^+$ lanes) DNA products generated by replisomes in the absence of primase (odd lanes) and in its presence (even lanes) using DnaB^{dilated} (lanes 1–2), DnaB^{wt} (lanes 3–4), and DnaB^{constr} (lanes 5–6) helicases.

In the co-crystal structure of the *Geobacillus stearothermophilus* DnaB$_6$(DnaGC)$_3$ complex, the three C-terminal domains of primase each bind to two adjacent subunits of the dilated hexameric collar domain in DnaB (***Figure 6.S5A***). However, in the constricted conformation of *Aquifex aeolicus* DnaB (***Figure 6.1B***, right panel), one of the two asymmetric DnaGC contact points in DnaB is buried and unavailable for binding to DnaG (Strycharska et al., 2013). In agreement with the structural considerations, it was further reported that DnaB^{dilated} is able to interact with DnaG and support priming activity whereas DnaB^{constr} could not sustain priming at all. We compared the activities of the three helicases in a bulk leading- and lagging-strand replication assay (***Figure 6.2E***, DnaG$^+$ path) and found that unlike DnaB^{wt} and DnaB^{dilated}, DnaB^{constr} was indeed unable to sustain OF synthesis upon addition of DnaG (***Figure 6.2F***; lane 6 *cf.* lanes 4 and 2). All three helicases, instead, proved proficient in leading-strand synthesis (***Figure 6.2E***, DnaG$^-$ path, and ***Figure 6.2F***, lanes 1, 3, and 5). Considering that DnaB^{wt} appears to be predominantly in the constricted state in solution, the observation that DnaB^{wt} supports the production of OFs strongly suggests the helicase is able to explore dilated-like states during replication. Thus, either the presence of primase or ssDNA, or both, enables DnaB to transition to the dilated state.

To test the possibility that DnaG binding to DnaB is sufficient to trigger the conformational transition in the helicase, we produced DnaGC (Loscha et al., 2004), a C-terminal domain of primase that holds all the determinants for DnaB binding but lacks the two N-terminal domains responsible for recognition of priming sites on DNA and RNA synthesis. Both DnaG and DnaGC interact similarly weakly with DnaB^{wt} with K_D values of 2.8 and 4.9 μM in 150 mM NaCl, respectively (Oakley et al., 2005). Injection of 0.5 μM DnaB^{wt} together with 5 μM DnaGC and 1 mM ATP (50 mM NaCl) over bio-τ_3CLC (***Figure 6.S4A***) resulted in a much higher response compared to the injection of DnaB^{wt} alone (***Figure 6.S4A***). This stronger binding was not ATP nucleotide specific, since the use of ADP resulted in the similar response (***Figure 6.S4B***). Injection of 5 μM DnaGC alone did not yield a detectable response, showing that the signal is not caused by direct binding of DnaGC to bio-τ_3CLC (***Figure 6.S4A***). Critically, fast-off kinetics are detected when DnaGC is absent during the dissociation of DnaB from the CLC, as if the DnaGC were not present during the association phase at all (***Figures 6.S4A*** *cf.* ***6.2B***). Considering that DnaGC appears to

dramatically increase the affinity of DnaB for CLC, the detected fast dissociation appeared to violate the basic thermodynamic principles that each ligand (CLC or DnaGC) must increase the affinity of protein (DnaB) for the other. To further investigate this, we measured binding of DnaB^{wt} to immobilised τ_3CLC by fixing the solution [DnaB^{wt}] to 100 nM while titrating DnaGC in the range from 0.5–8 μM (***Figure 6.S4C***). In spite of the three binding sites on DnaB for DnaGC, the data were reliably fit using an SSA model for one-to-one binding, as if only one of the three sites on DnaB has been titrated by DnaGC in the measured concentration range. The measured K_D of 1.74 ± 0.09 μM and the fast kinetics were similar to the previously reported binding of DnaB^{wt} to individual immobilised DnaG subunits (Oakley et al., 2005). These observations can be reconciled in a model that describes a cooperative transition in DnaB, with the weak binding of the first DnaGC initiating a conformational transition in the DnaB hexamer from constricted to a dilated state with at least 10–100-fold higher affinities for the second (and third) DnaGC.

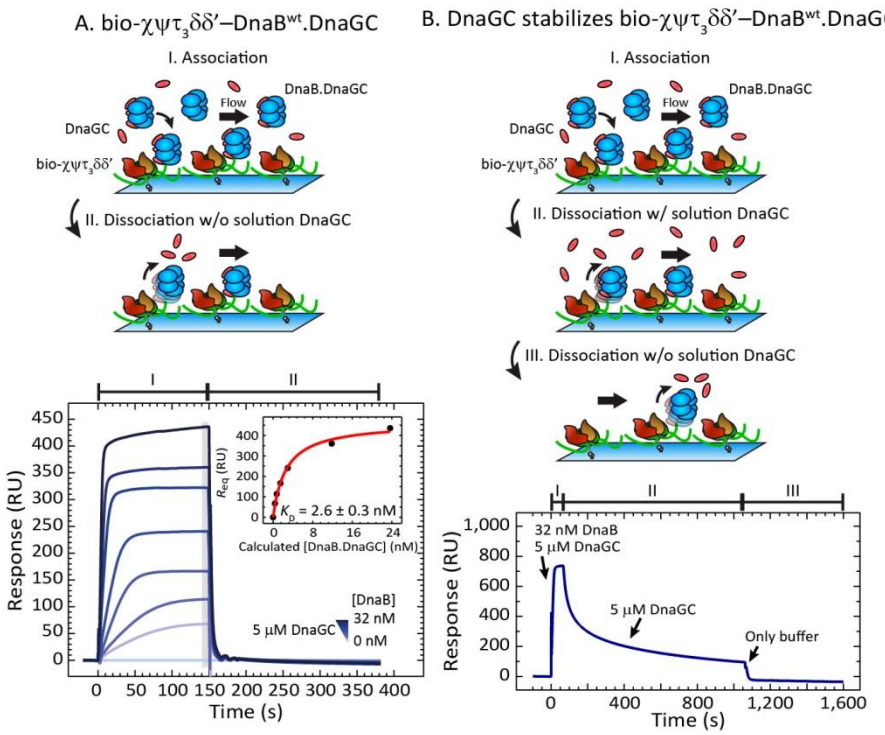

Figure 6.3: Association between DnaB and DnaGC strengthens the bio-χψτ3δδ'–DnaB interaction 500 fold

(A) Top panel: Cartoon presentation of the association and dissociation phases of an SPR experiment used to measure the binding of DnaB^{wt} in solution to immobilised τ_3CLC in the presence of DnaGC during association only. Bottom panel: SPR sensorgrams showing association (for 150 s) and dissociation of DnaB.DnaGC to and from bio-χψτ3δδ' obtained at optimized

0.5–32 nM range of serially diluted DnaB^{wt} samples containing 5 μM DnaGC, including zero. The responses at equilibrium R_{eq}, determined by averaging values in the grey bar regions of the sensorgrams, were fit (inset, red curve) against the calculated DnaB^{wt}.DnaGC concentrations (0–23.7 nM, see *6.4 Materials and Methods*) using an SSA model to obtain a K_D value of 2.6 ± 0.3 nM and an R_{max} value of 460 ± 10 RU. Errors are standard errors of the fit. (B) Top panel: Cartoon presentation of the association (with DnaGC) and two dissociation phases (with and without DnaGC, respectively) of an SPR experiment presented in the panel below. Bottom panel: DnaGC slows down the dissociation of DnaB^{wt} from bio-χψτ$_3$δδ′. SPR sensorgram shows the association of DnaB^{wt}.DnaGC during 60 s injection of 32 nM DnaB^{wt} in the presence of 5 μM DnaGC, followed by the 1,000 s dissociation in the presence of 5 μM DnaGC and second dissociation step without DnaGC.

The strength of the interaction between τ$_3$CLC and the DnaB^{wt}.DnaGC complex can be determined accurately by measuring responses at equilibrium for various concentrations of DnaB^{wt} in the presence of 5 μM DnaGC and fitting against the calculated concentration of DnaB^{wt}.DnaGC (see ***Equation 6.2*** in *6.4 Materials and Methods*) using an SSA model (K_D = 2.6 ± 0.3 nM; ***Figure 6.3A***). Likewise, binding of DnaB^{wt} to τ$_1$CLC at 5 μM DnaGC was similarly strong (K_D = 10 ± 1 nM; ***Figure 6.S4D***), again arguing that a single τ subunit within the τ$_3$CLC is responsible for helicase binding. Nevertheless, the increase in the strength of DnaB^{wt}–CLC interaction by up to ~500-fold in the presence of DnaGC indicates that the binding of the primase triggers the conformational switch in DnaB from the constricted to a dilated state, stabilising its binding to CLC. As expected, injection of DnaB^{constr} in the presence of DnaGC resulted in a much weaker response, consistent with its locked conformation and reduced ability to interact with primase (***Figure 6.S4E***).

In contrast, the presence of DnaGC (5 μM) in the dissociation phase strongly slows down the bio-τ$_3$CLC–DnaB dissociation to display a lifetime of several 100s of seconds (***Figure 6.3B***). These observations indicate that the DnaB conformation is regulated by primase–helicase interaction, thereby controlling the affinity of DnaB to the CLC. On the other hand, CLC cannot lock DnaB in its dilated state. We thus identified two functional forms of the helicase–clamp loader interaction: one with a weak affinity with the helicase in the constricted-like state and the other with a strong affinity that depends exclusively on (cooperative) primase–helicase interactions.

6.2.3 The strong helicase–clamp loader interaction stimulates the activity of a destabilized replisome

The τ subunit of the CLC has a central linking role in the replisome, connecting the polymerase core with the replicative helicase. Hence, a primase-induced >400-fold increase in DnaB–CLC affinity and strongly altered kinetics could be expected to significantly affect

the organisation and dynamics of the replisome. To demonstrate the importance of the strong helicase–clamp loader interaction in a functional context, we first turned to a rolling-circle leading-strand bulk replication assay (***Figure 6.2E***, DnaG^{-} path). In this traditional assay, the β_2–Pol III^{lead}–CLC–DnaB connectivity stimulates the simultaneous unwinding of dsDNA by DnaB and primer extension DNA synthesis by Pol III^{lead} core bound to the leading strand. We modified the assay such that the stability of Pol III* on DNA is compromised by leaving out the processivity factor β_2 in the reaction (***Figure 6.4A***). This condition artificially elevates the importance of the remaining DnaB–$\tau_3\delta\delta'$ link and allows us to visualize its functional dependence on the DnaGC concentration, [DnaGC]. Because of the expected inefficiency of the reaction, we first performed a time-course assay at constant DnaGC (2 μM) (***Figure 6.4B***, lanes 2–5). We find that the reaction still progresses and that the products are best observable at 80 min, with progressively longer products synthesised and more DNA templates consumed in time. Moreover, in the absence of DnaGC, replication was significantly less efficient and equivalent to the level in the DnaGC-dependent reaction at early time points (***Figure 6.4B***, lane 6 *cf.* lanes 2 and 3). The narrow distribution of product sizes points to the distributive nature of the DNA-synthesis process, not surprisingly considering the absence of β_2. Performing the reaction at progressively increasing [DnaGC] confirms a dependence of the synthesis efficiency on DnaGC (***Figure 6.4C***, lanes 1–5). Considering that (a) DnaGC has no enzymatic activity, (b) leading-strand replication does not proceed in the absence of the physical coupling between the helicase and Pol III* (Kim et al., 1996; Kornberg and Baker, 1991), (c) helicase-independent Pol III strand displacement synthesis cannot occur in the absence of β_2 (Jergic et al., 2013; Yuan and McHenry, 2009), (d) the efficiency of the replication increases in the range of [DnaGC] that is relevant for its interaction with DnaB (***Figure 6.S4C***) and stabilisation of the DnaB–CLC interaction (***Figure 6.3***), (e) helicase loading, presumably occurring via sliding onto the free 5'-end of the lagging strand, was unaffected by increase in [DnaGC] (as observed by a constant template utilisation as a function of [DnaGC]), and (f) DnaB was reported to be stable on ssDNA for very long periods [~60 min (Pomerantz and O'Donnell, 2010)], we conclude that the progressively higher efficiencies in DNA synthesis are due to a DnaGC-induced strengthening of the Pol III*–DnaB interaction.

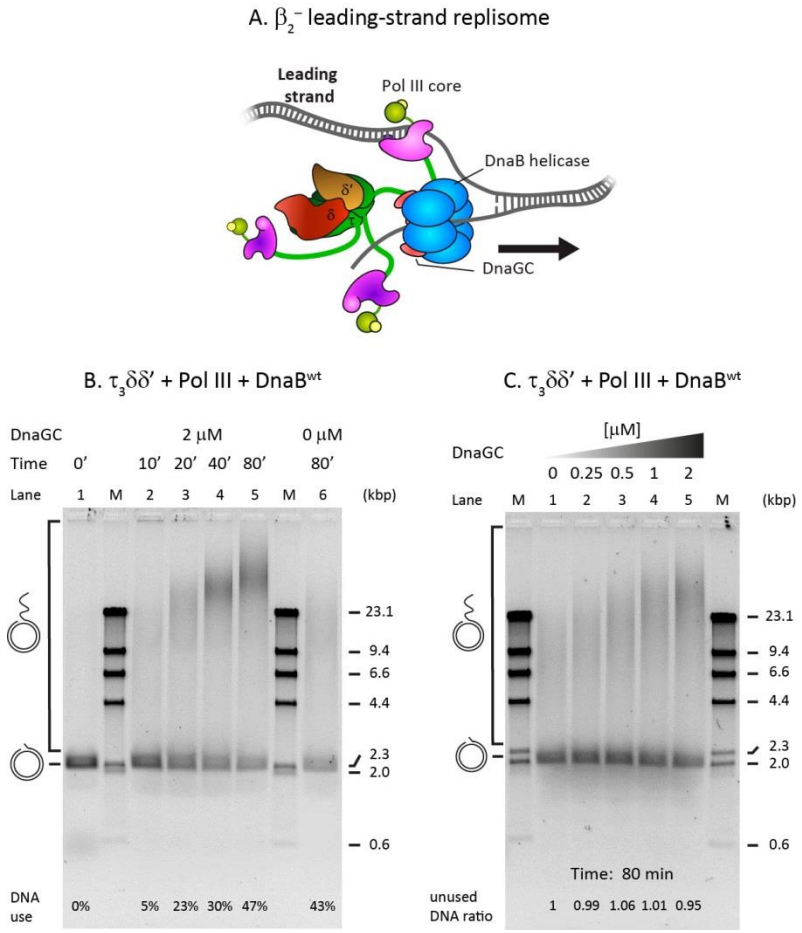

Figure 6.4: A strong DnaGC-induced CLC–DnaB interaction stimulates DNA replication in absence of the clamp

(A) Cartoon of the replisome that synthesises the leading strand only in the absence of β_2 clamp, as used in (B) and (C). (B) The time course of rolling-circle DNA synthesis reactions by the β_2^- replisome, at indicated time points, in the presence of 2 μM DnaGC (lanes 1–5) and in its absence (lane 6) are resolved on a 0.66% agarose gel. (C) Serially diluted DnaGC samples (0.25–2 μM, including zero) were supplemented into the individual rolling circle replication reactions and the replication products visualised on a gel after 80 min (lanes 1–5).

6.2.4 Binding of primase does not inhibit DnaB helicase activity

It is unknown whether the helicase stalls during priming in *E. coli*. It is also not known how long the primase is bound to the helicase during each OF cycle. As such, it is of importance to know whether the helicase–primase interaction stalls the helicase. Major experimental challenges in characterizing the DNA-unwinding activity of a helicase-primase

complex are the multivalent and weak nature of the interactions and the different helicase conformations. We used a disulphide cross-linked construct $DnaB_6^{F102C}$~$DnaGC_3^{R568C/C492L}$ (DnaB~GC) to remove the stoichiometric heterogeneity of DnaB–$(DnaGC)_n$ (n = 0–3) species and to ensure that helicase remains continuously in the dilated state with strong affinity for the CLC. The $DnaB^{F102C}$ is a mutant version of $DnaB^{wt}$ that interacts >200-fold less efficiently with DnaGC. Likewise, $DnaGC^{R568C/C492L}$ interacts with $DnaB^{wt}$ 30-fold more weakly compared to wild type. Nevertheless, the disulfide crosslinking efficiency between these mutants is nearly 100%, ensuring that for each hexamer of DnaB, essentially all three primase sites are occupied by DnaGC (Lo et al., unpublished).

To characterise DnaB~GC, we used SPR to monitor binding of DnaB~GC to bio-τ_3CLC. This experiment results in the characteristically slow dissociation (***Figure 6.5A***) that we previously observed with $DnaB^{dilated}$ (***Figure 6.2D***) or $DnaB^{wt}$ in the presence of DnaGC (***Figure 6.3B***). Moreover, similarly to $DnaB^{wt}$ and $DnaB^{constr}$, $DnaB^{F102C}$ exhibited a much lower response at equilibrium, accompanied by fast on and fast off kinetics (***Figure 6.5A***). These data indicate that DnaB~GC is indeed in a dilated state and interacts strongly with the CLC.

We next used DnaB~GC in our leading-strand assay lacking the β_2 processivity clamp and compared its activity against a $DnaB^{F102C}$ control (with and without DnaGC; ***Figure 6.5B***). We reasoned that if the activity of the DnaB~GC driven replisome is found to be similar to or stronger than those of controls, it would indicate that DnaB remains an active helicase even when primases are bound to it. The control lanes show that $DnaB^{F102C}$ is active (***Figure 6.5B***, lane 1) while the presence of 2 μM DnaGC makes no difference to yield and product length (***Figure 6.5B***, lane 2). No change in activity is expected because of the much weaker affinity of the mutant helicase for the primase. However, the presence of DnaB~GC in the reaction results in higher replication efficiency compared to control lanes (***Figure 6.5B***, lane 3 *cf.* lanes 1, 2). Considering that the template consumption was similar across reactions, our results show that DnaB is an active helicase when it is bound to all three DnaGCs, further confirming that the dilated state is functional. Interestingly, leading-strand assays in the presence of the β_2 clamp revealed that replisomes with DnaB~GC do not appear to be more efficient than with $DnaB^{F102C}$ (***Figure 6.S5B***). This result suggests that if Pol III on the leading strand is stabilised by interactions with β_2, the strengthening of the DnaB–CLC interaction becomes less critical for the stability of β_2–Pol III^{lead}–CLC–DnaB. Taken together, we conclude that DnaB shows helicase activity in both constricted and dilated states (***Figure 6.5C***), even when bound to its binding partners within the replisome.

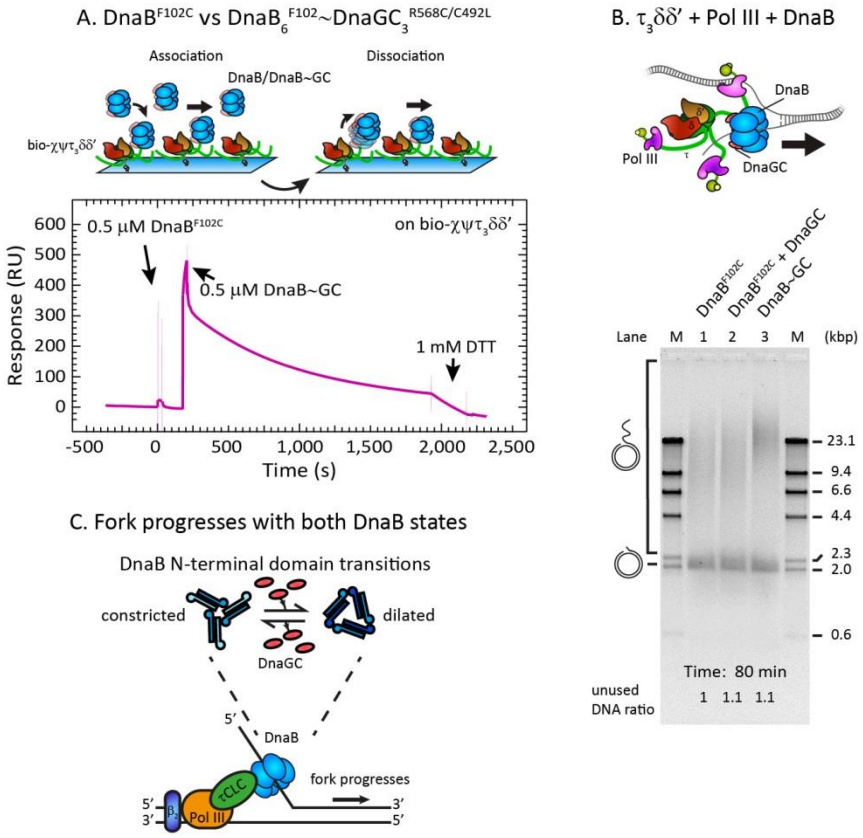

Figure 6.5: Cross-linked DnaB~GC complex is an active helicase

(A) Top panel: Cartoon representation of association and dissociation phases of an SPR experiment designed to visualise the binding of cross-linked DnaB~GC to immobilised τ_3CLC. Bottom panel: SPR sensorgrams showing association and dissociation profiles of consecutive injections of $DnaB^{F102C}$ alone and cross-linked $DnaB_6^{F102C}$~$DnaGC_3^{R568C/C492L}$ (DnaB~GC) on bio-$\chi\psi\tau_3\delta\delta'$. During DnaB~GC dissociation, dithiothreitol (DTT) injected at ~1,800 s reduces the disulphide cross-linking bond, leading to release of DnaGCs and faster dissociation. Spikes in the signal corresponding to imperfect signal subtraction from the control flow cell during solution changes are made more transparent to highlight the relevant portions in the sensorgrams. (B) Rolling-circle leading-strand replication reactions in the absence of β_2 were supplemented with $DnaB^{F102}$ (lane 1), $DnaB^{F102}$ and 2 μM DnaGC (lane 2), and DnaB~GC (lane 3) and the products were separated on a 0.66% agarose gel following 80 min reaction. (C) Concluding cartoon illustration of the leading-strand synthesis, which occurs irrespective of the conformation of DnaB N-terminal domains.

6.2.5 DnaG concentration controls the number of Pol III*s associated with the replisome

The replication assays discussed above enabled us to detect functional differences and similarities in partial replisomes as a function of the strength of DnaB–CLC interaction. Next, we set out to examine the role of the conformational switch in the helicase on full replisome activity by real-time, single-molecule observations of replication. We previously reported the use of a single-molecule rolling-circle assay to image fluorescently labelled Pol III* complexes associated with the replisome and visualise dynamic exchange of replisome-bound Pol III*s with those in solution on the timescale of seconds (Lewis et al., 2017). We hypothesized that [DnaG]-induced strengthening of the DnaB–CLC interaction could contribute to the accumulation of Pol III*s at the replication fork by slowing down the exchange, and conversely, a weakening could promote exchange and lower the steady-state population.

We employed single-molecule FRAP (fluorescence recovery after photobleaching) experiments (Lewis et al., 2017) and measured the recovery time of fluorescent signal upon photobleaching due to the turnover of fluorescently labelled Pol III* at the replication fork at different [DnaG] (30, 70, 150, and 300 nM) as both leading and lagging strands are replicated (***Figure 6.6A***). The population of labelled Pol III*s in the field of view was photobleached every 20 s with 2-s pulses at high laser power (***Figure 6.6B***, top panel) and the recovery of intensity of the fluorescent Pol III* signal at the fork tracked as a function of time after each high-power pulse (***Figure 6.6B***, bottom panel). Fluorescence intensities were converted into numbers of Pol III*s by calibrating the intensity of a single labelled Pol III*, as described before (Lewis et al., 2017). To analyse the data, we pooled together every recovery interval in which we observed replication (***Figure 6.6C***; red circles) for a particular [DnaG] (***Figure 6.6C***) and fit (***Figure 6.6C***; blue curve) their averaged fluorescence intensity values (***Figure 6.6C***; black squares) with a FRAP recovery equation (***Equation 6.3***). This procedure was repeated for each [DnaG] (***Figures 6.6D and 6.S6A–C***).

Our single-molecule analysis revealed that the characteristic exchange time (exchange lifetime, *T*) increases with [DnaG] in a concentration range that is physiologically relevant (***Figure 6.6E***, left panel). This observation of Pol III* stabilization at the fork with increasing [DnaG] can readily be explained by DnaB spending more time in a dilated-like state as [DnaG] increases, leading to progressively slower exchange kinetics. In addition, extrapolation of *T* to zero as [DnaG] approaches zero implies that the translocating DnaB resumes the constricted-like state on DNA as it unwinds dsDNA in the absence of DnaG–DnaB contacts. Further, our data reveal that the number of replisome-associated Pol III*s at 100 nM DnaG, the concentration found in the cell (Rowen and Kornberg, 1978), is two to three, increasing to four copies at 300 nM DnaG (***Figure 6.6E***, right panel). Fitting the number of exchanged Pol III* against [DnaG] to a steady-state equation (***Equation 6.4***) shows that the maximum number of associated Pol III* could be as high as six (***Figure 6.6E***, right panel). The K_M extracted from these data is 90 $\pm$ 30 nM, ~30-fold below the K_D of the

DnaB–DnaG interaction [2.8 μM (Oakley et al., 2005)] but reasonably close to the K_M value for primer utilisation [17 ± 3 nM (Graham et al., 2017)]. This observation suggests that the transition to dilated-like state(s) depends on additional interactions of DnaG in the replisome, presumably with the lagging strand template (*i.e.*, during priming events).

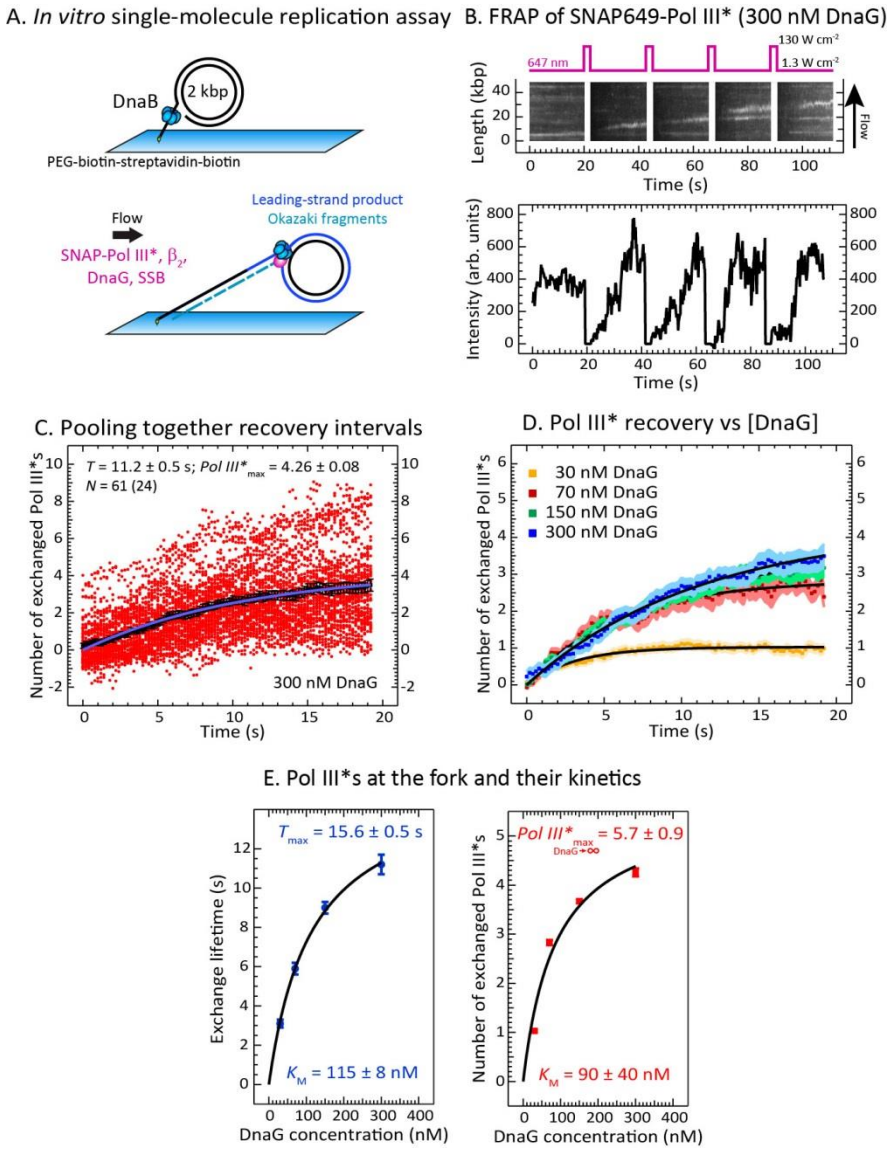

Figure 6.6: Single-molecule FRAP experiments: DnaG stimulates accumulation of polymerases and slows down their exchange dynamics at the replication fork

(A) Cartoon showing the two stages of the single-molecule leading and lagging rolling-circle DNA synthesis assay. First, 2-kbp rolling-circle substrate with DnaB loaded at its 5'-end tail is bound to a coverslip surface through

biotin-streptavidin bond. Then SNAP-Pol III*, β_2, DnaG, and SSB are flowed in to initiate replication. (B) Top panel: a representative kymograph of SNAP-Pol III* at the replication fork in the presence of 300 nM DnaG. Every 20 s, a 2-s high power pulse laser is used to photobleach the population of SNAP-Pol III* in the field of view. Bottom panel: recovery of SNAP-Pol III* intensities over time for an individual active replisome. (C) 61 intensities (red circles) obtained from the recovery intervals of 24 replisomes at 300 nM DnaG are converted into the number of exchanged Pol III* and displayed, together with their average values (black square). Fitting the evolution of average recovery intensities in time with the FRAP recovery equation (***Equation 6.3***) provides the characteristic (exchange) time (T = 11.2 $\pm$ 0.5 s), the maximum number of exchanged Pol III* (*Pol III**$_{max}$ = 4.26 $\pm$ 0.08), and the remaining background intensity y_0, converted in number of Pol III*s (y_0 = 0.72 $\pm$ 0.04), then subtracted from every other curve. (D) Averaged recovery intensities at each DnaG concentration (30, 70, 150, and 300 nM) and their FRAP recovery fit curves (black) are shown. The remaining values for the T, *Pol III**$_{max}$, and y_0 are presented in ***Figure 6.S6***. (E) T (left panel) and *Pol III**$_{max}$ (right panel), plotted as a function of DnaG concentration, are fitted with a steady-state equation (***Equation 6.4***) providing the K_Ms (115 $\pm$ 8 nM and 90 $\pm$ 40 nM, respectively) and either the maximum exchange lifetime (T_{max} = 15.6 $\pm$ 0.5 s, left panel) or the maximum number of exchanged Pol III* (*Pol III**$_{max,\ DnaG\rightarrow\infty}$ = 5.7 $\pm$ 0.9, right panel) as DnaG approaches infinity.

6.3 Discussion

In this report, we present evidence for at least two functional modes of interaction between the bacterial clamp loader and helicase, CLC–DnaB, corresponding to different conformations of the N-terminal collar in DnaB. We first isolated and characterised CLCs on the surface of an SPR chip (***Figures 6.S1 and 6.S2***), then demonstrated that binding between CLC and DnaB^{wt} is weak and transient in nature (***Figures 6.2B and 6.S3C***). In solution, DnaB appears to be predominantly in a constricted-like state (***Figure 6.1B***, right panel), considering that its affinity for the CLC (***Figure 6.2B***) is not much different (~2.5-fold less) from DnaB^{constr} (***Figure 6.2C***). In the constricted conformation, one of the two contact regions in the pair of adjacent monomers of the DnaB hexamer responsible for the asymmetric interaction with DnaG is sterically inaccessible. Consistent with this structural picture, the conformationally-constrained DnaB^{constr} did not support priming and OF synthesis (***Figure 6.2F***). However, in the dilated conformation, DnaB^{dilated} interacts strongly with the CLC and the complex is slow to dissociate (***Figure 6.2D***). Binding of DnaGC promotes the conformation in DnaB with high affinity to the CLC so that binding affinity increases >400-fold (***Figures 6.3A and 6.S4D***). Nevertheless, the dissociation of DnaB from

the CLC is still fast in the absence of DnaGC in solution while DnaB–DnaGC binding is unaffected by the presence of CLC in the high range of [DnaGC] [***Figure 6.S4C*** and (Oakley et al., 2005)]. Taking into account the multiplicity of the DnaB–DnaGC interaction, we believe that this outcome is possible only if positively cooperative binding of multiple DnaGCs is involved, with the conformational switch initiated by binding of the first DnaGC to DnaB. However, in the presence of high DnaGC (5 μM), the dissociation of DnaB from CLC is slow (***Figure 6.3B***), similar to the dissociation of $DnaB^{dilated}$ (***Figure 6.2D***). We thus conclude that binding of the primase induces the conformational change in the replicative helicase from a constricted-like state with low affinity for CLC to a dilated-like state with a high affinity for the CLC.

Next, we demonstrated the functional significance of high DnaB–CLC affinity in a modified leading strand DNA synthesis assay in the absence of the processivity factor, the β_2 sliding clamp (***Figure 6.4A***). Sliding clamps are utilised in all domains of life to stabilise polymerases as they translocate on DNA between successive nucleotide incorporation steps. We hypothesised that the intentional weakening of Pol III core binding to DNA due to the absence of clamp might expose the relative change in strength of other contributing interactions, *i.e.* that of DnaB–CLC. Indeed, this was the case: strengthening of the DnaB–CLC interaction in the presence of increasing [DnaGC] led to more efficient DNA synthesis (***Figures 6.4B and 6.4C***) whereas template utilisation was not affected (***Figure 6.4C***).

The precise mechanism by which the *E. coli* replisome coordinates repetitive lagging-strand priming with DNA synthesis on both leading and lagging strands is not known (Dixon, 2009). One possibility is that the helicase pauses during primer synthesis – a hypothesis based on initial single-molecule studies of the phage T7 replication system (Lee et al., 2006) and later inferred from *E. coli* leading-strand synthesis studies in the presence of DnaG or DnaGC (Tanner et al., 2008). Another scenario is that the helicase continues unimpeded unwinding of dsDNA at the fork as it remains in contact with the primase that is bound to the priming sequence on the lagging strand. This mechanism results in the temporary formation of a "priming loop" that collapses as the new primer is handed off from the primase to polymerase (Manosas et al., 2009; Pandey et al., 2009). A critical difference between these mechanisms is the ability of the primase to modulate the helicase activity, in particular whether DnaB helicase pauses when it is bound to primase. To answer this question, we utilised the cross-linked DnaB~GC (Lo et al., unpublished) and used SPR measurements to show that binding of DnaB~GC to the CLC is strong while the dissociation from the CLC is slow (***Figure 6.5A***). These observations suggest that DnaB is in the dilated conformation, as expected for the DnaGC-bound form. We then tested the activity of DnaB~GC in leading-strand synthesis, both in the absence (***Figure 6.5B***) and presence of the clamp (***Figure 6.S5B***), and confirmed that DnaB remains an active helicase, both in the constricted conformation (***Figure 6.2F***, lanes 5,6), and in the dilated form linked to DnaGC and strongly associated to the CLC. Our findings thus suggest that the formation of priming loops in *E. coli* is possible, and if it does not happen, there must be a rather specific mechanism in place to prevent it.

Finally, we demonstrated the significance of the DnaG-induced conformational switch in the helicase in the context of full replisomes during active DNA synthesis. We measured the recovery of fluorescence intensity at the replication fork following photobleaching (***Figure 6.6B***). Our measurements revealed that the maximum number of replisome-associated Pol III* increases as [DnaG] increases from 30 to 300 nM. In the physiological range of [DnaG] (50–100 nM), there are on average 2−3 exchangeable Pol III* complexes residing at the fork (***Figures 6.6C, 6.6D, and 6.S6***). Fitting the maximum number of associated Pol III* against [DnaG] revealed that the upper limit of associated Pol III* at the fork is ~6 (***Figure 6.6E***, right panel). In addition, a similarity in trends of both the exchange lifetime *T* (***Figure 6.6E***, left panel) and the number of associated Pol III*s at the fork (***Figure 6.6E***, right panel) to increase with rising [DnaG] can be rationalised by slowing down of the CLC–DnaB dissociation with DnaG bound (***Figures 6.3B*** *cf.* ***6.2B***). These trends suggest that higher [DnaG] increases the portion of time that the helicase spends in dilated- rather than constricted-like states. Conversely, the trend in the fit of *T versus* [DnaG] towards lower concentrations suggests a zero exchange time in the absence of DnaG, implying that under those conditions, the actively translocating helicase resumes a constricted-like state. Using a very different approach, a model proposed by Strycharska et al., 2013 also predicted that DnaB would be in the constricted state except when it contacts DnaG for priming.

While the single-molecule photobleaching experiments are performed at physiologically relevant [DnaG], the Pol III* concentration in those assays (3 nM) is lower than what is found inside the cell [~25 nM (Lewis et al., 2017)]. We chose this lower concentration to enable experimental access to exchange times across the entire range of tested [DnaG] (30−300 nM). The *T* we measured at 300 nM DnaG of 11.2 ± 0.5 s was consistent with the previous measurements (11.0 ± 0.6 s) under the same conditions (Lewis et al., 2017). Those measurements also determined a ~6-fold reduction in *T* upon increasing [Pol III*] from 3 to 13 nM. At 70 nM DnaG, a concentration approximate to that found in the cell (Rowen and Kornberg, 1978), we measured *T* to be ~6 s, so a reduction of *T* to around one second and an increase in the number of exchangeable Pol III* to >3 can be expected at physiological Pol III* and DnaG concentrations. These numbers would suggest that the exchange lifetime per individual associated Pol III* molecule (*T* divided by Pol III*$_{max}$) is well below one second and on par with the OF cycle time.

The value for the K_D measured for the DnaG–DnaB interaction [2.8 μM (Oakley et al., 2005)] is much higher than the K_M (90 ± 40 nM) we observe in the [DnaG]-dependent exchange process. This discrepancy exposes the role of other interactions that DnaG establishes in the replisome that are important for exchange. Taking into account the uncertainty and the different origin of the observables we measure, the fitted K_M is reasonably close to the K_M value for primer utilisation (~20 nM) measured by others (Graham et al., 2017). These observations underscore the critical role of interaction between DnaG and the lagging-strand template for the primase-induced conformational switch in the helicase. This global CLC–DnaB interaction framework ensures that Pol III* is

not sequestered by helicase in solution and would instead be preferentially bound by a translocating helicase at the apex of the fork that is engaged in interactions with primase.

So why would there be a need for DnaG priming as a signal that triggers a helicase conformational change that in turn recruits Pol III*s to the vicinity of the replication fork? One obvious possibility is that a Pol III* newly recruited to DnaB could participate downstream in the primase-to-polymerase switch (Yuzhakov et al., 1999) and subsequent OF synthesis, operating in conjunction with a different Pol III* that is already replicating the leading strand. Such a model with multiple Pol III* complexes acting at the fork would allow for a large number of scenarios describing polymerase behaviour in replication, including Pol III* being left behind on a nascent OF and the simultaneous synthesis of multiple OFs (Duderstadt et al., 2016; Geertsema et al., 2014).

In enzymology, proteins are known to form symmetrical assemblies that undergo cooperative allosteric transitions thereby serving as switches that allow one molecule in the cell to affect the fate of another (Alberts et al., 2007). Switches are often selected to enable a tight, ligand-concentration dependent regulation that cannot otherwise be achieved with a single protein. The cooperative allosteric regulation of a DnaG-induced conformational switch in *E. coli* DnaB appears to be capable of functioning as a temporal switch, selected by evolution to support timely engagement of new Pol III*s into the DNA synthesis process. For example, simultaneous binding of primase to the exposed site in constricted DnaB and to DNA (*i.e.*, during primer synthesis) enables titration under physiological conditions of the weak (first) DnaG binding site. Subsequently, the helicase undergoes a cooperative allosteric transition to a dilated state and increases its affinity of the remaining two sites for the primase. This in turn greatly increases the affinity of the helicase for the CLC, resulting in rapid accumulation of Pol III*s at the replication fork. However, upon separation from the primer, the primase rapidly separates from the weak binding site, reversing the initial allosteric transition towards the constricted state and weakening the other two primase binding sites in the helicase. This switch would result in rapid dissociation of Pol III*s from the helicase and its further handoff to a primed site for OF synthesis (primase-to-polymerase switch).

Further work is necessary to deduce whether the proposed primase-to-polymerase switch via the DnaG-induced conformational change in the helicase represents a mechanism that is regularly utilised in OF synthesis, or whether it serves as a backup mechanism to handle roadblocks and obstructions, *i.e.* when priming on the leading strand becomes necessary or when there are delays in the recycling of the lagging-strand polymerase. The first possibility would appear to be in strongest agreement with the recent paradigm shift in the field proposing a rather stochastic behaviour of Pol III* at the replication fork, with new Pol III*s dynamically exchanging in the replisome while DnaB remains stably associated at the fork (Beattie et al., 2017; Geertsema and van Oijen, 2013; Graham et al., 2017; Lewis et al., 2017; Monachino et al., 2017; van Oijen and Dixon, 2015; Q. Yuan et al., 2016). Interestingly, the T7-phage employs a similar strategy of accumulation of polymerases (gp5) on the helicase fused to the primase (gp4) for prompt primer handoff

(Geertsema et al., 2014; Loparo et al., 2011). The observation of similar mechanisms in systems of such different complexity suggests that the accumulation of polymerases at the replication fork for a primer handoff could be a conserved mechanism in nature.

6.4 Materials and Methods

6.4.1 Reagents

Chemicals: (±)-6-hydroxy-2,5,7,8-tetramethylchromane-2-carboxylic acid (Trolox; Sigma-Aldrich), glacial acetic acid (Ajax Finechem), ADP (Sigma-Aldrich), agarose (Bioline), ATP (Sigma-Aldrich), biotin-PEG-SVA (Laysan Bio, Inc.), catalase (Sigma-Aldrich), dNTPs (dATP, dCTP, dGTP, dTTP) (Bioline), dithiothreitol (Astral Scientific), EDTA (Ajax Finechem), glucose monohydrate (Sigma-Aldrich), glucose oxidase (Sigma-Aldrich), HCl (Ajax Finechem), potassium (K-)glutamate (Sigma-Aldrich), $MgCl_2$ (Ajax Finechem), $Mg(OAc)_2$ (Sigma-Aldrich), mPEG-SVA (Laysan Bio, Inc.), NaCl (Sigma-Aldrich), Na_2EDTA (Ajax Finechem), NaOH (ChemSupply), surfactant P20 (GE Healthcare), PDMS (Ellsworth), rNTPs (ATP, CTP, GTP, UTP) (Bioline), SDS (Sigma-Aldrich), Tris (Astral Scientific and Sigma-Aldrich), Tween-20 (Sigma-Aldrich).

Gel Electrophoresis: agarose gel loading dye (6x) alkaline (Boston BioProducts), 6x DNA Gel Loading Dye (ThermoFisher Scientific), 10,000x SybrGold (LifeTechnology), GeneRuler DNA Ladder mix (ThermoFisher Scientific), lambda DNA/*Hin*dIII Marker (ThermoFisher Scientific).

6.4.2 Buffers

ALEM buffer*:** 2x agarose gel loading dye (6x) alkaline, 200 mM EDTA; ***alkaline buffer*:** 50 mM NaOH, 1 mM EDTA; ***imaging buffer: 30 mM Tris.HCl, pH 7.6, 12 mM $Mg(OAc)_2$, 50 mM K-glutamate, 0.5 mM EDTA, 0.0025% (*v*/*v*) Tween-20, 0.5 mg/mL BSA, 1 mM freshly made UV-aged Trolox, 0.45 mg/mL glucose oxidase, 0.024 mg/mL catalase, 0.8% (*w*/*v*) glucose monohydrate, 10 mM dithiothreitol, 1.25 mM ATP, 0.25 mM each UTP, CTP, and GTP, 50 μM each dATP, dTTP, dCTP, and dGTP; ***LES buffer*:** 2x DNA Gel Loading Dye, 200 mM EDTA, 2% SDS; ***neutralization buffer*:** 1 M Tris.HCl, pH 7.6, 1.5 M NaCl; ***replication buffer A*:** 30 mM Tris.HCl, pH 7.6, 12 mM $Mg(OAc)_2$, 50 mM K-glutamate, 0.5 mM EDTA, 0.0025% (*v*/*v*) Tween-20; ***replication buffer B*:** 30 mM Tris.HCl, pH 7.6, 12 mM $Mg(OAc)_2$, 50 mM K-glutamate, 0.5 mM EDTA, 0.0025% (*v*/*v*) Tween-20, 0.5 mg/mL BSA; ***SPR1 buffer*:** 50 mM Tris.HCl, pH 7.6, 200 mM NaCl, 10 mM $MgCl_2$, 0.25 mM dithiothreitol, 0.005% (*v*/*v*) P20; ***SPR2 buffer*:** 25 mM Tris.HCl, pH 7.6, 50 mM NaCl, 5 mM $MgCl_2$, 0.25 mM dithiothreitol, 0.005% (*v*/*v*) P20; ***Tris acetate EDTA (TAE) buffer*:** 40 mM Tris, 20 mM acetic acid, 1 mM EDTA (final pH 8.3).

6.4.3 Proteins

E. coli replication proteins and protein complexes were purified according to previously published protocols: $\tau_2\gamma_1\delta\delta'$, $\tau_3\delta\delta'$, $\chi\psi\tau_3\delta\delta'$ (Tanner et al., 2008), DnaB and DnaC (San Martin et al., 1995), $\gamma_3\delta\delta'$ and DnaBC (Jergic et al., 2013), $\alpha\varepsilon\theta$ and SNAP649-$\alpha\varepsilon\theta$ (Lewis et al., 2017), β_2 (Oakley et al., 2003), DnaB^{constr} and DnaB^{dilated} (Strycharska et al., 2013), DnaG (Stamford et al., 1992), DnaGC (Loscha et al., 2004), DnaB^{F102C} and DnaB~GC (Lo et al., unpublished), and SSB (Mason et al., 2013). Detailed procedures for production of bio-χ and bio-$\chi\psi$ are described in *6.5 Supplementary Material*. Isolation of bio-$\chi\psi\tau_3\delta\delta'$ and bio-$\chi\psi\tau_1\gamma_2\delta\delta'$ (***Figure 6.S3A***) followed methods for production of non-biotinylated CLCs (Tanner et al., 2008).

6.4.4 Bulk DNA replication assays

Ensemble-averaging (bulk) DNA replication experiments aimed at comparing activities of DnaB^{dilated} and DnaB^{constr} in the context of both leading-strand synthesis and simultaneous leading- and lagging-strand synthesis were commenced by mixing on ice in replication buffer A in 10 μL reaction volume: 3.8 nM biotinylated flap-primed 2-kb circular DNA template (Monachino et al., 2018), 1.25 mM ATP, 250 μM each UTP, CTP, and GTP, 200 μM each dATP, dTTP, dCTP, and dGTP, 30 nM $\chi\psi\tau_3\delta\delta'$, 90 nM Pol III, 200 nM β_2, 60 nM DnaB^{wt}, DnaB^{constr} or DnaB^{dilated}, and 360 nM DnaC. When specified, 300 nM DnaG was used for RNA priming on the lagging strand, allowing lagging-strand synthesis to proceed. Since DnaB^{constr} does not load efficiently in the presence of SSB (not shown), the reactions were initiated in a water bath at 37°C for 1 min in absence of SSB to preload helicases. Following the addition of 50 nM SSB, reactions were incubated at 37°C for a further 14 min. In this way, differences in efficiencies of DNA synthesis among the reactions containing different DnaB versions are mainly due to the elongation phase and not to the loading efficiency. Reactions were quenched by mixing equal volumes of replication solution with ALEM buffer, followed by heating in a water bath at 70°C for 5 min and prompt cooling on ice for at least 3 min. Reaction products were then resolved by alkaline agarose gel electrophoresis in 0.5% (*w*/*v*) agarose gel; 4 μL GeneRuler DNA Ladder mix in 1x agarose gel loading dye (6x) alkaline (final volume: 12 μL) were loaded as markers. The alkaline agarose gels were soaked for at least 1 h in alkaline buffer before the reaction products and the markers were loaded. Gels were run at 15 V for ~15 h in a Mini-Sub Cell GT System (Bio-Rad). Then, gels were neutralized in neutralization buffer for ~2 h, and stained with 1x SybrGold in 2x TAE buffer for 7 h. The SybrGold-stained DNA molecules were detected with a Bio-Rad Gel Doc XR (302 nm trans-UV light; ***Figure 6.2F***).

Bulk leading-strand replication reactions in the absence of β_2 clamps were assembled by mixing on ice in replication buffer A in 10 μL final reaction volume: 3.8 nM biotinylated flap-primed 2-kb circular DNA template (Monachino et al., 2018), 1 mM ATP, 400 μM each dATP, dTTP, dCTP, and dGTP, 30 nM $\tau_3\delta\delta'$, 90 nM Pol III, 30 nM DnaB^{wt}, DnaB^{F102C} or DnaB~GC, and, unless otherwise stated, 10 mM dithiothreitol (***Figures 6.4B***

and 6.4C). DnaGC concentration is declared in each experiment. Dithiothreitol was omitted in the reactions that compare the activities of DnaB~GC with DnaB^{F102C} to avoid reduction of the disulphide crosslink in DnaB~GC (***Figure 6.5B***). Unless differently declared, reactions were incubated in a water bath at 30°C for 80 min, then quenched by mixing equal volumes of replication solution and LES buffer. Reaction products were separated by gel electrophoresis in 0.66% (*w*/*v*) agarose gels; 0.1 μL lambda DNA/*Hin*dIII Marker in 1x DNA Gel Loading Dye (final volume: 4 μL) were loaded as marker. Lambda DNA/*Hin*dIII Marker was previously treated according to manufacturer recommendations (it was heated in a water bath at 65°C for 5 min, followed by incubation in ice for at least 3 min). Gels were run in 2x TAE buffer for 100 min at 75 V in a Mini-Sub Cell GT System (Bio-Rad), followed by staining with 1x SybrGold (LifeTechnology) in 2x TAE buffer for 2 h. The SybrGold-stained DNA molecules were detected with a Bio-Rad Gel Doc XR (302 nm trans-UV light).

Time course bulk leading-strand synthesis reactions with DnaB^{F102C} and DnaB~GC in the presence of β_2 were assembled as follows: a 60 μL-master-mix containing 3.8 nM biotinylated flap-primed 2-kb circular DNA template (Monachino et al., 2018), 1 mM ATP, 400 μM each dATP, dTTP, dCTP, and dGTP, 30 nM $\tau_3\delta\delta'$, 90 nM Pol III, 200 nM β_2, and 30 nM DnaB^{F102C} or DnaB~GC was prepared by mixing components in replication buffer A on ice; 10 μL were removed for each condition and mixed with 10 μL of LES buffer to provide the 0 time-point. The remaining volumes were transferred in a water bath at 37°C. At indicated time-points, 10 μL were removed for each condition and mixed with 10 μL of LES buffer to quench reactions. Reaction products were separated by gel electrophoresis in 0.66% (*w*/*v*) agarose gels; 1.5 μL GeneRuler DNA Ladder mixes in 1x DNA Gel Loading Dye (final volume: 12 μL) were loaded as markers. Gels were run in 2x TAE buffer for 150 min at 60 V in a Wide Mini-Sub Cell GT System (Bio-Rad), followed by staining with 1x SybrGold (LifeTechnology) in 2x TAE buffer for 2 h. The SybrGold-stained DNA molecules were detected with a Bio-Rad Gel Doc XR (302 nm trans-UV light; ***Figure 6.S5B***).

6.4.5 Identification and quantification of DNA bands in gels

Quantification of DNA bands in gels was performed using GE Healthcare Life Sciences "Image Quant TL" (*v.* 8.1). Lanes were manually identified. The "rubber band" background subtraction algorithm was used. The bands corresponding to the 2-kb DNA template were manually detected and their intensity was calculated by the software (***Figures 6.4B, 6.4C, 6.5B, and 6.S5B***).

6.4.6 Surface plasmon resonance (SPR) experiments

SPR experiments were carried out on a BIAcore T100/T200 (GE Healthcare) or on a 6 x 6 multiplex BioRad ProteOn XPR-36 system at 20°C, unless stated. On the BIAcore, a SA (streptavidin-coated) sensor chip (GE Healthcare) was activated with three sequential injections of 1 M NaCl, 50 mM NaOH (40 s each at 5 μL/min). Likewise, all 36 interaction spots on a ProteOn NLC (neutravidin-coated) sensor chip were conditioned with three

sequential injections of 1 M NaCl, 50 mM NaOH across six vertical (ligand) flow paths (40 s each at 40 μL/min) and six horizontal (analyte) flow paths (40 s each at 100 μL/min).

The stability tests of CLC on the surface of BIAcore T100 SA-coated sensor chip were performed at 5 μL/min flow using buffer SPR1. Measurements were initiated by immobilising ~700 RU of bio-χψ (133 s injection at 325 s, step 1 in ***Figures 6.S1A and 6.S1B***), followed by association of $\tau_3\delta\delta'$ at 100 nM (1,500 s injection at 789 s, step 2 in ***Figures 6.S1A and 6.S1C***). Dissociation, monitored over the period of more than 5,000 s, was interspersed by injections of: (a) SPR1 buffer + 1 mM ADP (120 s injection at 3,110 s, ***Figure 6.S1C***), (b) 1 M $MgCl_2$ (60 s injection at 3,554 s, step 3 in ***Figures 6.S1A and 6.S1D***), (c) solution of δ (550 nM) and δ′ (900 nM) in buffer SPR1 (75 s injection at 4,010 s, step 4 in ***Figures 6.S1A and 6.S1E***), (d) 1 M $MgCl_2$ (60 s injection at 4,554 s, step 5 in ***Figure 6.S1A***), (e) solution of δ′ (900 nM) in buffer SPR1 (75 s injection at 4,733 s, step 6 in ***Figures 6.S1A and 6.S1F***), and (f) the same solution as in (e).

Considering that the bio-χψ chip surface could not efficiently be regenerated, binding kinetics parameters for bio-$\chi\psi$–$\tau_2\gamma_1\delta\delta'$ and bio-$\chi\psi$–$\gamma_3\delta\delta'$ interactions in the absence and presence of ATP (***Figure 6.S2***) were determined using single-shot measurements of the reaction kinetics on a ProteOn NLC sensor chip, designed to provide detailed kinetic analysis in a single injection cycle without regeneration between samples. Following immobilisation of bio-χψ in the ligand direction, the chip was rotated 90°, and solutions of serially-diluted $\tau_2\gamma_1\delta\delta'$/$\gamma_3\delta\delta'$ samples in each case (0.625–10 nM, including zero) in buffer SPR1 (or SPR1 supplemented with 1 mM ATP) were made to flow simultaneously through all six horizontal (analyte) channels at 30 μL/min for 700 s. Dissociation of bound molecules was monitored in the same buffer over 6,000 s. For each round of measurements, bio-χψ was re-immobilised on a new ligand flow path. The final sensorgrams were unmodified ligand flow path- and zero-subtracted using ProteOn Manager Software (*v.* 3.1.0.6). Equilibrium (dissociation constant K_D) and kinetic parameters (rate constants, k_a and k_d) were determined by simultaneous fitting of the five sensorgrams per measured interaction from the optimised concentration range using a 1:1 (Langmuir) binding model incorporated in BIAevaluation software (*v.* 4.0.1).

All other interactions that enabled determination of dissociation constants (K_D) for CLC–$DnaB^{wt}$ and mutant DnaB versions, in the absence and presence of DnaGC, as well as CLC.$DnaB^{wt}$–DnaGC were characterised using a BIAcore T200 instrument. First, bio-$\chi\psi\tau_1\gamma_2\delta\delta'$ and bio-$\chi\psi\tau_3\delta\delta'$ were immobilised on two flow cells of a SA sensor chip to 1,400 and 1,450 RU, respectively, in running buffer SPR2 supplemented with 0.2 mM ATP for stabilisation of CLCs on the sensor chip surface. Binding studies were initiated by sequential injections of solutions of serially-diluted $DnaB^{wt}$ samples from the optimised concentration range (0.0625–8 μM, including zero) in buffer SPR2 + 0.2 mM ADP at 30 μL/min for 30 s. While ADP stabilises the DnaB hexamer and does not influence measured values of binding at equilibrium (R_{eq}) compared to ATP, it was found to reduce unspecific interactions at high [DnaB] and formation of species that were slow to dissociate, which becomes a critical contribution because CLCs on the chip surface cannot be regenerated. Sensorgrams were

zero-subtracted and R_{eq} values, generated by averaging response values in the grey highlighted region from the appropriate DnaB concentration range, were fitted against [DnaB] using a 1:1 SSA model incorporated in the BIAevaluation software (*v.* 4.0.1) (***Figures 6.2B, 6.2C and 6.S3C***):

$$R_{\mathrm{eq}} = R_{\max}\left(\frac{[A]}{[A]+K_{\mathrm{D}}}\right) \qquad \text{(Equation 6.1)}$$

where R_{max} corresponds to the response when all the immobilized ligands on the surface are saturated with the analyte A, and [A] is the concentration of analyte in solution.

The τ_3CLC–DnaB^{constr} interaction was measured under similar conditions, including the utilised analyte concentration range, except that the temperature was 25°C (***Figure 6.2C***). The τ_3CLC.DnaB–DnaGC interaction was also studied under similar conditions by sequential injections of solutions containing fixed (100 nM) DnaB and serially-diluted DnaGC samples from the optimised concentration range (0.0625–4 μM, including zero; ***Figure 6.S4C***) at 30 μL/min for 30 s. Analyses of the data were performed using the SSA model as described above. In contrast, preliminary analysis showed that DnaB^{dilated} binds much more strongly to τ_3CLC, with very different kinetics parameters, so for illustrative purposes 250 nM DnaB$_6^{dilated}$ was injected for 400 s under the same conditions used in case of DnaB^{constr}, and the slow dissociation was recorded for over 2,500 s (***Figure 6.2D***).

For measurement of the K_D(bio-$\chi\psi\tau_3\delta\delta'$–DnaB^{wt}.DnaGC) and K_D(bio-$\chi\psi\tau_1\gamma_2\delta\delta'$–DnaB^{wt}.DnaGC) interactions, a range of solutions of serially-diluted DnaB^{wt} samples (0.5–64 nM, including zero) in the presence of 5 μM DnaGC were injected at 30 μL/min for 150 s over immobilised bio-$\chi\psi\tau_3\delta\delta'$ (1,800 RU) and bio-$\chi\psi\tau_1\gamma_2\delta\delta'$ (1,630 RU), in SPR2 buffer containing 0.2 mM ATP and 0.2 mM EDTA, followed by flow of the same running buffer. Given that we varied [DnaB], whereas the DnaB.DnaGC complex and not DnaB titrates the immobilised ligand in the low-nM range of utilised DnaB, and that CLC does not affect DnaB–DnaGC interaction, the concentration of DnaB.DnaGC in solution was obtained by solving the quadratic equation for *x* derived from ***Equation 6.2***:

$$\frac{([\mathrm{DnaB}]_0 - x)([\mathrm{DnaGC}]_0 - 3x)}{x} = K_{\mathrm{D}}(\mathrm{DnaB\text{–}DnaGC}) \qquad \text{(Equation 6.2)}$$

where *x* is solution [DnaB.DnaGC], $[DnaB]_0$ and $[DnaGC]_0$ are the initial concentrations of DnaB and DnaGC (a constant value, equal to 5 μM), respectively, whereas the K_D(DnaB–DnaGC) is the dissociation constant for the interaction of DnaB with DnaGC (1.74 ± 0.09 μM, ***Figure 6.S4C***). This equation is derived based on 1:1 interaction between the DnaB and the first weakly bound molecule of DnaGC, a property previously also observed by Oakley et al. (2005), in the background of positive cooperative interaction with the second and third DnaGC that each bind >10-fold more strongly compared to the first one (three DnaGCs allosterically bind to DnaB). Given the appropriate range of 0.5–32 nM of serially-diluted $[DnaB]_0$ made to flow over τ_3CLC or (0.5–64 nM in case of τ_1CLC), ***Equation 6.2*** was used to

calculate the concentration of solutions of DnaB.DnaGC samples that were injected over immobilised ligand: 0, 0.4, 0.7, 1.5, 3.0, 5.9, 11.8 and 23.7 nM in case of τ_3CLC (***Figure 6.3A***), and an extra 47.1 nM injection in case of τ_1CLC (***Figure 6.S4D***).

To study how the presence of DnaGC affects dissociation of DnaB from CLC, 32 nM $DnaB^{wt}$ with 5 μM DnaGC were injected over immobilised τ_3CLC in buffer SPR2 containing 0.2 mM ATP and 0.2 mM EDTA at 5 μL/min for 60 s, and then the solution of 5 μM DnaGC in the same buffer was coinjected for 1,000 s immediately following the protein association phase to monitor the dissociation of DnaB. Finally, the remaining proteins were washed with the SPR2 running buffer (***Figure 6.3B***). In addition, similar conditions were used to test binding of $DnaB^{F102C}$ or disulphide-bond cross-linked DnaB~GC with immobilised τ_3CLC, except that the proteins (0.5 μM each) were subsequently injected at 30 μL/min for 30 s, and the dissociation of DnaB~GC monitored for 1,720 s, followed by injection for 250 s of the buffer in use that was additionally supplemented with 1 mM dithiothreitol to uncouple $DnaB^{F102C}$ from $DnaGC^{R568C/C49L}$, stimulating the dissociation of $DnaB^{F102C}$ (***Figure 6.5A***).

6.4.7 *In vitro* single-molecule fluorescence recovery after photobleaching (FRAP) experiments

In vitro single-molecule FRAP experiments were performed similarly to a previously published investigation (Lewis et al., 2017). Briefly, a microfluidic flow cell was obtained by positioning a PDMS flow chamber on top of a PEG-biotin-functionalized microscope coverslip. To reduce non-specific interactions of proteins and DNA molecules with the surface, the chamber was blocked with replication buffer B. The flow-cell was placed on an inverted microscope (Nikon Eclipse Ti-E, Japan) with a CFI Ap TIRF 100x oil-immersion TIRF objective (1.49 NA, Nikon, Japan) and connected to a syringe pump (New Era Pump Systems Inc., Adelab Scientific, Australia) for flow of buffer. Flow-cell temperature was maintained at 31°C by an electrically heated chamber (Okolab, Burlingame, CA).

Leading- and lagging-strand replication experiments were performed under continuous presence of all proteins except DnaBC and as a function of [DnaG] in the 30−300 nM range. Briefly, 40 nM DnaBC was incubated with 340 pM biotinylated flap-primed 2-kb circular DNA template (Monachino et al., 2018), 10 mM dithiothreitol, and 1 mM ATP in replication buffer B for 3 min in a water bath at 37°C. This mixture was then diluted 10 times to a final volume of 220 μL, and loaded into the flow cell first at 40 μL/min for 2.5 min, then at 10 μL/min for 7.5 min, and finally in absence of flow for few minutes (***Figure 6.6A***, top panel). During the loading process, the imaging buffer was made. SNAP-Pol III* was assembled *in situ* by incubating 280 nM τ_3CLC with 850 nM SNAP649-Pol III in imaging buffer for 90 s in a water bath at 37°C. Finally, the replication solution, which contained 1 mM freshly made UV-aged Trolox, 0.45 mg/mL glucose oxidase, 0.024 mg/mL catalase, 0.8% (*w/v*) glucose monohydrate, 10 mM dithiothreitol, 1.25 mM ATP, 0.25 mM each UTP, CTP, and GTP, 50 μM each dATP, dTTP, dCTP, and dGTP, 3 nM SNAP-Pol III*, 40 nM β_2, 250 nM SSB, and 30, 70, 150, or 300 nM DnaG in replication buffer B, was loaded into the flow

cell first at 20 μL/min for 3.5 min, then at 10 μL/min until end of the experiment (***Figure 6.6A***, bottom panel).

The fluorescently-labelled Pol III* was visualized by excitation with a 647 nm laser (Coherent, Obis 647–100 CW) at 1.3 W/cm^2 (photo-bleaching lifetime was 40 s). Every 20 s, every Pol III* in the field of view was photo-bleached with a 2-s pulse at 130 W/cm^2 (photo-bleaching lifetime was 0.7 s) (***Figure 6.6B***, top panel). Imaging was done with an EMCCD (Photometrics, Tucson, AZ; 512 Delta). The camera allowed a resolution of 160 nm/px. Because of the high efficiency of *E. coli* DNA replication, only one field of view per experiment was recorded for 5 min. Each experimental condition was examined at least twice.

The analysis was done with Fiji, using in-house built plugins and macros. Briefly, using Fiji, every field of view was corrected to account for background and beam profile. Individual replicating DNA molecules were manually located. Then, the position of the fluorescently-labelled Pol III* at the tip was semi-manually tracked (***Figure 6.6B***, top panel) and its integrated intensity calculated in a 5-px-by-5-px square, applying a local background subtraction (***Figure 6.6B***, bottom panel). By calibrating the intensity of a single SNAP649-Pol III, we could convert intensities into number of Pol III*s. At a fixed DnaG concentration, only those recovery intervals where replication occurred were averaged together and fit with the following FRAP recovery function (***Equation 6.3***):

$$Pol\ III^* = y_0 + Pol\ III^*_{\max}\left(1 - e^{-\frac{t}{T}}\right) \qquad \text{(Equation 6.3)}$$

where *Pol III**$_{max}$ is the maximum number of exchanged *Pol III**, *T* is the characteristic exchange time, and y_0 accounts for incomplete background removal and was further subtracted from recovery intervals (***Figures 6.6C, 6.6D, and 6.S6A–C***). We averaged recovery intervals from at least 21 individual DNA molecules. Error bars to the averaged values are standard error of the mean (normalized to the number of recovery intervals). The resulting *Pol III**$_{max}$ and *T*, plotted against DnaG concentration, were fit with a steady-state affinity function (***Equation 6.4***):

$$y = y_{\max}\left(\frac{[DnaG]}{[DnaG]+K_M}\right) \qquad \text{(Equation 6.4)}$$

where y_{max} represents the maximum value reached by *y* (either *Pol III**$_{max}$ or *T*) when the concentration of DnaG approaches infinity, while K_M is an apparent dissociation constant of DnaG (***Figure 6.6E***).

6.5 Supplementary Material

6.5.1 Plasmid construction

pSJ1376 (bio-χ): The plasmid pET-χ (Xiao et al., 1993) that directs overproduction of full-length χ was a kind gift of Dr. Mike O'Donnell. It was used as a template for PCR amplification of the *holC* gene (encoding χ) using primer 108 (5'-AAA AAA AAC ATA TGA AAA ACG CGA CGT TCT ACC TTC TGG), designed to incorporate a Met^1 start codon as part of the *Nde*I site just before the Lys^2 codon of *holC*, and primer 109 (5'-TTG AAT TCT TAT TTC CAG GTT GCC GTA TTC AGG), that incorporates an *EcoR*I restriction site just following the TAA stop codon. The PCR product was isolated after digestion with *Nde*I and *EcoR*I and inserted between the same set of restriction sites in plasmid pKO1274 (Jergic et al., 2007). Vector pKO1274, a derivative of pETMSCI (Neylon et al., 2000), allows fusion of the gene in-frame behind a sequence encoding an N-terminal biotinylation tag [sequence MAGLNDIFEAQKIEWHEH (Beckett et al., 1999)] using an *Nde*I restriction site. The resulting plasmid pSJ1376 places the *bio-χ* gene under the transcriptional control of the bacteriophage T7 ϕ10 promoter, which in *E. coli* BL21(λDE3) strains enables bio-χ protein overproduction by addition of isopropyl-β-D-thiogalactoside (IPTG).

6.5.2 Overproduction and purification of bio-χ

E. coli strain BL21(λDE3)/pLysS/pSJ1367 was grown at 37°C in LB medium supplemented with thymine (25 mg/L), ampicillin (100 mg/L), chloramphenicol (30 mg/L) and 25 μM (D)-biotin, to A_{600} = 0.8. To induce overproduction of bio-χ, 0.75 mM IPTG was added to the shaking culture. Cultures were grown for a further 3 h, and then chilled in ice. Cells were harvested by centrifugation (11,000 x *g*; 6 min), frozen in liquid N_2 and stored at –80°C.

After thawing, cells (4.27 g, from 2 L of culture) were resuspended in 65 mL lysis buffer [50 mM Tris.HCl, pH 7.6, 2 mM dithiothreitol, 1 mM EDTA, 20 mM spermidine]. The cells were lysed by being passed twice through a French press (120,00 psi). Cell debris were removed from the lysate by centrifugation (30,000 x *g*; 30 min) to yield the soluble Fraction I. Proteins in Fraction I that were then precipitated by addition of solid ammonium sulphate (0.45 g/mL) and stirring for 60 min, were collected by centrifugation (35,000 x *g*; 30 min) and dissolved in 30 mL buffer A [30 mM Tris.HCl, pH 7.6, 1 mM dithiothreitol, 1 mM EDTA] containing 150 mL NaCl. The solution was dialysed against two changes of 2 L of the same buffer, to yield Fraction II.

Fraction II was applied at 1 mL/min onto a column (2.5 x 15 cm) of Toyopearl DEAE-650M resin that had been equilibrated with buffer A + 150 mM NaCl. Fractions containing bio-χ that did not bind to the resin were pooled and dialysed against two changes of 2 L of buffer A + 30 mM NaCl to yield Fraction III (note that we previously observed instability of χ when the buffer NaCl was < 20 mM).

The dialysate (Fraction III, 50 mL) was loaded at 1 mL/min onto the same DEAE

column that had been equilibrated with buffer A + 30 mM NaCl. The column was washed with the same buffer and bio-χ eluted between one- and three-column-volumes in a broad peak. Fractions containing bio-χ were pooled and dialysed against two changes of 2 L of buffer A + 30 mM NaCl to give Fraction IV.

The dialysate (Fraction IV, 120 mL) was loaded at 1 mL/min onto a column (2.5 x 10 cm) of Toyopearl SuperQ that had been equilibrated with buffer A + 30 mM NaCl. After washing the column with 60 mL of buffer A + 30 mM NaCl, bio-χ was eluted in a linear gradient (300 mL) of 30–160 mM NaCl in buffer A, in a single peak at ~70 mM NaCl. Fractions containing bio-χ were pooled and dialysed against two changes of 2 L of buffer A + 30 mM to give Fraction V.

Fraction V (35 mL) was loaded at 1 mL/min onto a column (2.5 x 15 cm) of heparin-Sepharose 4B [prepared as described (Wijffels et al., 2004)] that had been equilibrated with buffer A + 30 mM NaCl. The column was washed with the same buffer and bio-χ eluted between one- and three-column-volumes in a broad peak. This purification step did not contribute to improvement in the purity of the protein. Fractions containing bio-χ were pooled to give Fraction VI.

Proteins in Fraction VI (80 mL) were then precipitated by addition of solid ammonium sulphate (0.45 g/mL) and stirring for 60 min. Precipitated proteins were collected by centrifugation (35,000 x *g*; 30 min), then dissolved in 5 mL buffer A +100 mM NaCl and finally dialysed against the 2 L of the same buffer to yield Fraction VII (6 mL, containing 8 mg of the pure protein).

The molecular weight (MW) of purified bio-χ determined by nanoESI-MS in 1% formic acid solution containing 1 mM β-mercaptoethanol (18,650.8 ± 0.2 Da and 18,779.1 ± 0.1 Da) indicated that the N-terminal methionine had been partially removed (from ~80 % of the protein) and that biotinylation had not taken place, so the protein was biotinylated *in vitro*.

For *in vitro* biotinylation, one part of biomix buffer [50 mM Tris.HCl, 250 mM bicine, pH 8.3, 50 mM ATP, 50 mM magnesium acetate, 250 mM D-biotin] was mixed with three parts of substrate solution (Fraction VII, 70 μM bio-χ) in buffer A + 100 mM NaCl and one part of MilliQ water, and *E. coli* biotin ligase added to 0.8 μM in final volume of 6.8 mL biotinylation mix. The biotinylation mix was treated at 30°C for 3 h and then dialysed in 2 L of buffer buffer A + 100 mM NaCl at 6°C for storage, yielding Fraction VIII (7.5 mL, containing ~6 mg of the bio-χ in the presence of some biotin-ligase). Aliquots were first tested for stability upon freezing in liquid N_2 and, once the stability on freezing/thawing was confirmed, the protein was stored at –80°C.

The MW of *in vitro* biotinylated bio-χ determined by nanoESI-MS in 1% formic acid and 1 mM β-mercaptoethanol (18,877.1 ± 0.1 Da and 19,005.6 Da) compares well to the calculated value of 18,878 Da in the absence of Met^1 and 19,009 Da when Met^1 is present, assuming that biotin had been attached.

6.5.3 Preparation of bio-χψ complex

Refolding of ψ in the presence of bio-χ was carried out based on methods described in Tanner et al. (2008), with some modifications.

About 6 mL of bio-χ (~4.8 mg) in buffer A + 100 mM NaCl was added to 9 mL refolding buffer B [20 mM Tris.HCl, pH 7.6, 100 mM NaCl, 2 mM dithiothreitol, 0.5 mM EDTA] while stirring, followed by drop-wise addition of 1 mL of ψ in 6 M urea (~10 mg/mL). Consequently, the final concentration of urea in solution was ~0.4 M, a condition that allows ψ to fold and interact with χ. The solution was continued to stir for 4 h at 4°C and then dialysed overnight in 2 L of buffer C [25 mM Tris.HCl, pH 7.6, 90 mM NaCl, 2 mM dithiothreitol, 0.5 mM EDTA, 10% (*v/v*) glycerol].

Following dialysis, the solution was clarified by centrifugation (35,000 × *g*; 30 min) and the soluble fraction loaded at 1 mL/min onto a column (2.5 x 7 cm) of Toyopearl DEAE-650M resin that had been equilibrated in buffer C. After SDS-PAGE analysis on a 4–20% gel, fractions containing bio-χψ that did not bind to the column were pooled (12 mL, containing 4 mg of protein complex) and stored at –80°C.

6.6 Supplementary Figures

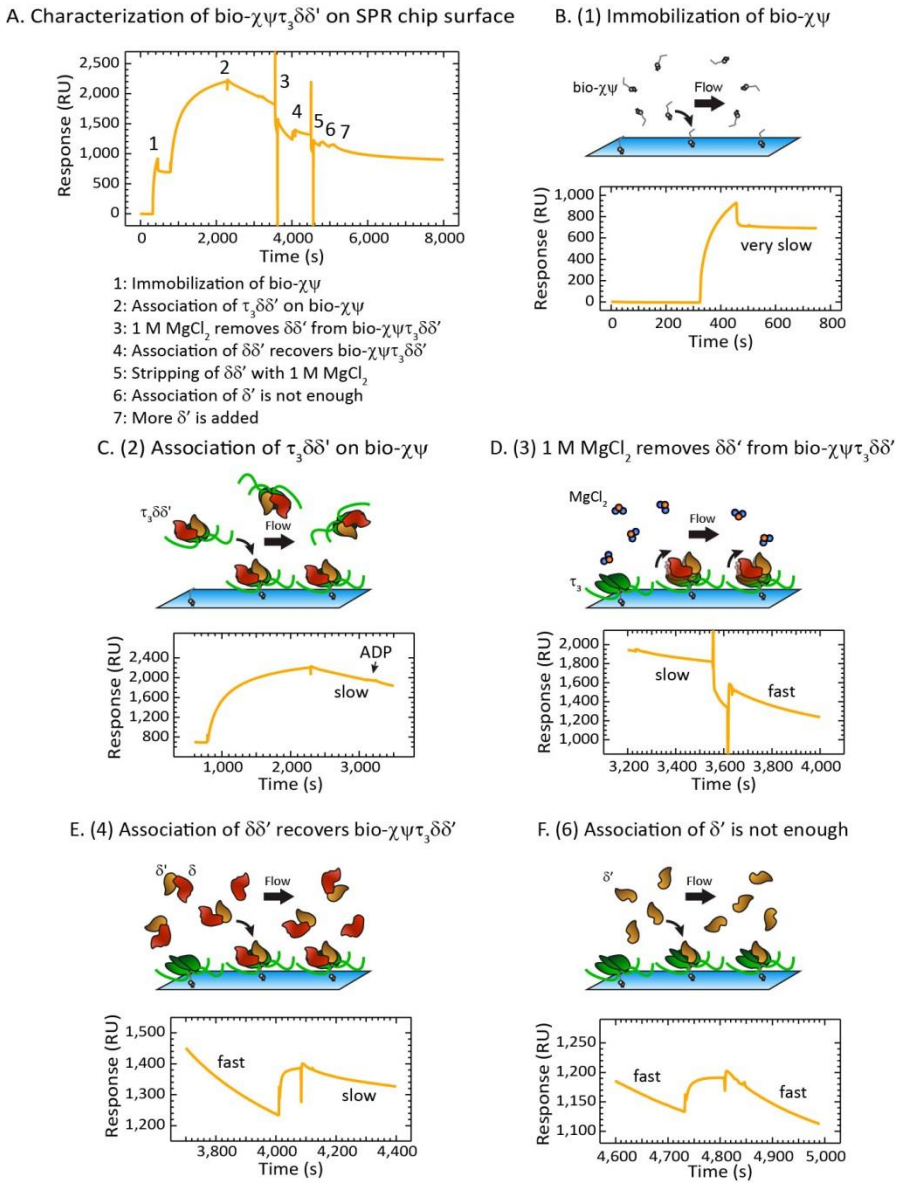

Figure 6.S1: Characterization of the stability of bio-χψτ₃δδ' on an SPR chip surface

Related to ***Table 6.1***. (A)–(F) Interrogation of bio-χψτ3δδ' stability was performed by monitoring association and dissociation phases as various proteins (in SPR1 buffer, containing 200 mM NaCl) and 1 M $MgCl_2$ were injected. (A) Steps in the τ3CLC assembly and its characterisation process. (B) First, bio-χψ was immobilized on the surface. Immobilised bio-χψ proteins are

stably bound and dissociation was very slow. (C) To assemble the entire CLC on the chip surface, 100 nM $\tau_3\delta\delta'$ in SPR1 buffer was injected for 1,500 s, and uninterrupted dissociation, monitored over ~900 s, allowed estimation of the dissociation half-life $t_{1/2}$ (~50 min). Injection of 1 mM ADP did not affect the dissociation rate. (D) Injection of 1 M $MgCl_2$ stripped only part of the mass from the surface and accelerated the dissociation rate ~5-fold ($t_{1/2}$ ~10 min). (E) While 75 s injection of saturating $\delta\delta'$ assembled *in situ* from 550 nM δ and 900 nM δ' allowed restoration of the slow dissociation rate ($t_{1/2}$ ~45 min), the injection of 900 nM δ' (F), shown to interact with τ_3 (Park et al., 2010), could not restore slow dissociation rate following re-treatment with 1 M $MgCl_2$. Our measurements are thus consistent with the dissociation of a wholesale $\tau_3\delta\delta'$ complex from immobilised bio-$\chi\psi$ in SPR1 buffer and, surprisingly, with the removal of $\delta\delta'$ from bio-$\chi\psi\tau_3\delta\delta'$ and dissociation of τ_3 from bio-$\chi\psi$ following the treatment with 1 M $MgCl_2$.

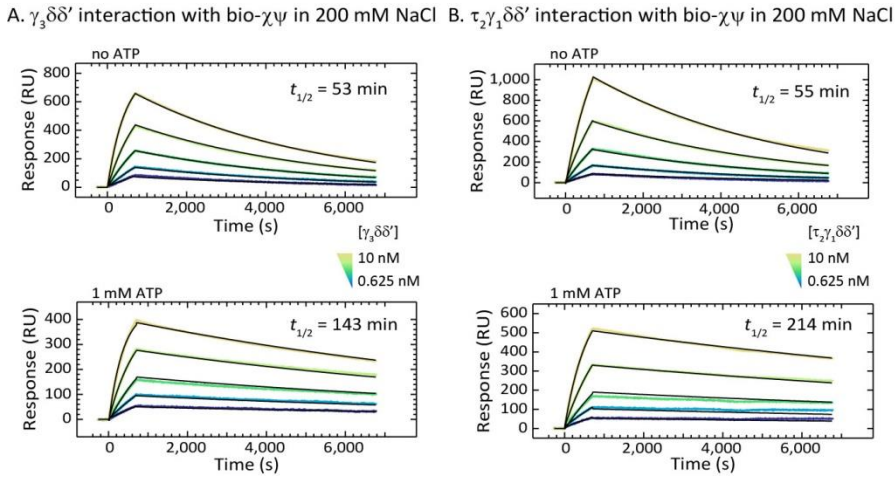

Figure 6.S2: ProteOn sensorgrams showing association and dissociation phases of bio-χψ–$\gamma_3\delta\delta'$ and bio-χψ–$\tau_2\gamma_1\delta\delta'$ interactions, in the presence or absence of ATP

Related to ***Table 6.1***. Solutions (0.625–10 nM, including zero) of $\gamma_3\delta\delta'$ (A) and $\tau_2\gamma_1\delta\delta'$ (B), with or without ATP, were injected over immobilised bio-$\chi\psi$ for 700 s, and dissociation was monitored over 6,000 s. Each group of five sensorgrams (shown in colours) were simultaneously (globally) fit (black curves) using a 1:1 (Langmuir) binding model to determine the corresponding binding parameters K_D, k_a, k_d, and $t_{1/2}$ values (***Table 6.1***).

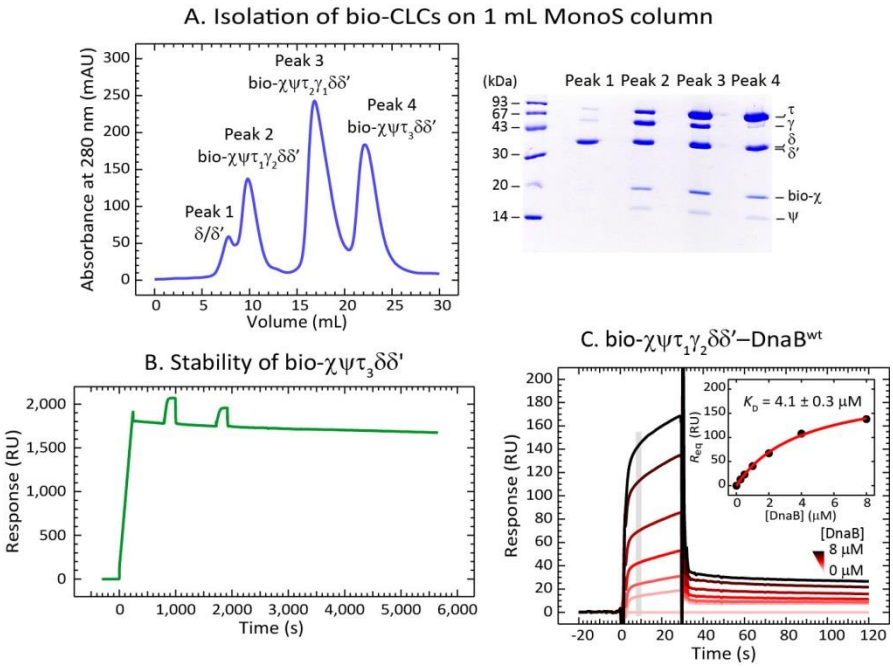

Figure 6.S3: Isolation of bio-CLCs and their use in SPR studies

Related to ***Figure 6.2***. (A) Isolation of bio-$\chi\psi\tau_1\gamma_2\delta\delta'$, bio-$\chi\psi\tau_2\gamma_1\delta\delta'$ and bio-$\chi\psi\tau_3\delta\delta'$ clamp loader complexes on a 1 mL MonoS 5/50 GL column (GE Healthcare). Samples from peaks (left panel) were analysed by 4–20% SDS-PAGE (right panel). (B) Bio-$\chi\psi\tau_3\delta\delta'$ was immobilized on a SA chip surface and its improved stability, manifested in slow dissociation in SPR2 buffer that contained reduced NaCl concentration (50 mM instead of 200 mM) and 1 mM ATP for stabilisation of the complex, was monitored for over an hour. Control injections of DnaB samples in the presence of DnaGC, which were followed by prompt and complete dissociation, confirmed the practical utility of our experimental strategy. (C) SPR sensorgrams show association and dissociation phases of bio-$\chi\psi\tau_1\gamma_2\delta\delta'$–DnaB^{wt} interaction at the optimized 0.25–8 μM range of serially diluted DnaB^{wt} sample, including zero. The responses at equilibrium, determined by averaging values in the grey bar region of the sensorgrams, were fit (inset, red curve) with an SSA model to obtain a K_D value of 4.1 ± 0.3 μM and an R_{max} value of 210 ± 7 RU. Errors are standard errors of the fit.

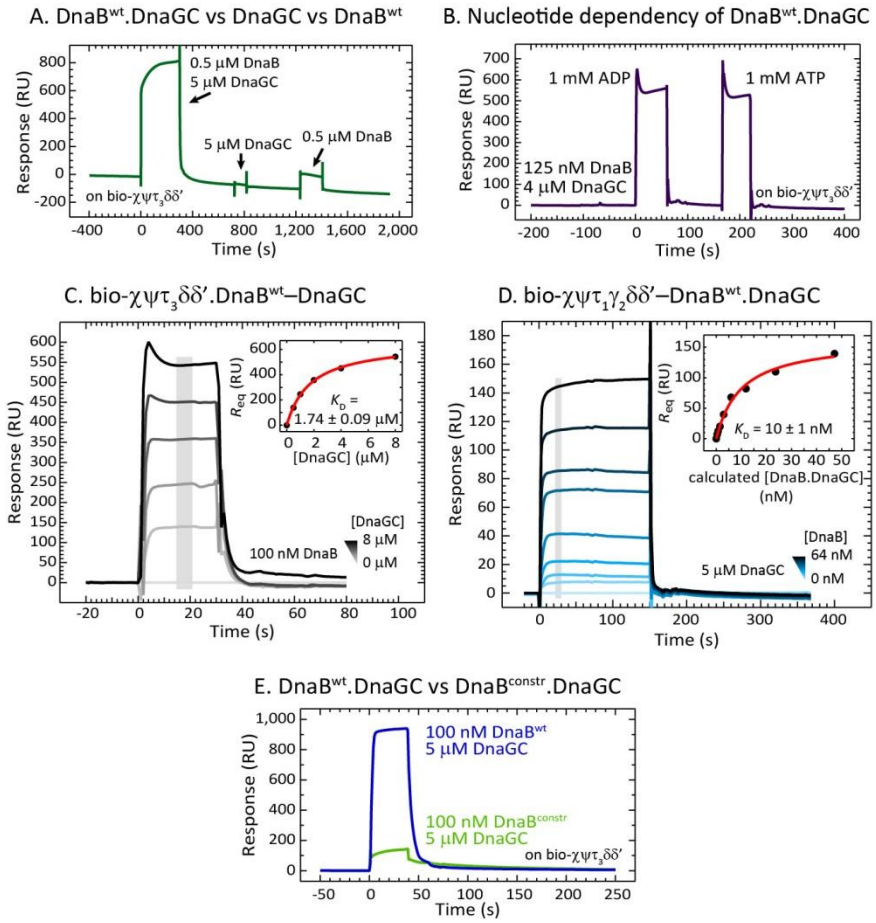

Figure 6.S4: Supplemental SPR studies of interactions between bio-CLC and DnaB variants in presence of DnaGC

Related to ***Figure 6.3***. (A) Preliminary SPR sensorgram obtained by consecutive injections of 0.5 μM DnaB^{wt} with 5 μM DnaGC, then of 5 μM DnaGC and finally of 0.5 μM DnaB^{wt} in SPR2 buffer with 1 mM ATP shows that while DnaGC stimulates binding of DnaB to immobilised bio-χψτ$_3$δδ′, it does not specifically or non-specifically bind to the ligand at utilised 5 μM concentration. (B) Under similar experimental conditions, there was no critical difference in SPR responses if 125 nM DnaB^{wt} and 4 μM DnaGC were injected with either 1 mM ADP or 1 mM ATP. (C) Sensorgrams showing association and dissociation of bio-χψτ$_3$δδ′.DnaB–DnaGC interaction at an optimized 0.5–8 μM range of serially diluted DnaGC samples, including zero, and constant 100 nM DnaB^{wt}. The responses at equilibrium, determined by averaging values in the grey bar region, were fit (inset, red curve) with an SSA to obtain a K_D value of 1.74 ± 0.09 μM and an R_{max} value of 660 ± 10 RU. Errors are standard errors of the fit. (D) Sensorgrams showing association and dissociation of bio-

$\chi\psi\tau_1\gamma_2\delta\delta'$–DnaB.DnaGC interaction at the optimized 0.5–64 nM range of serially diluted $DnaB^{wt}$ samples, including zero, and 5 μM DnaGC. The responses at equilibrium, determined by averaging values in the grey bar region, were fit (inset, red curve) against the calculated $DnaB^{wt}$.DnaGC concentrations (0–47.1 nM; see *6.4 Materials and Methods*) with an SSA model to obtain a K_D value of 10 ± 1.0 nM and an R_{max} value of 163 ± 7 RU. Errors are standard errors of the fit. (E) Comparison of SPR sensorgrams when 100 nM $DnaB^{wt}$ (blue curve) or 100 nM $DnaB^{constr}$ (green curve) were injected in the presence of 5 μM DnaGC over immobilised bio-$\chi\psi\tau_3\delta\delta'$.

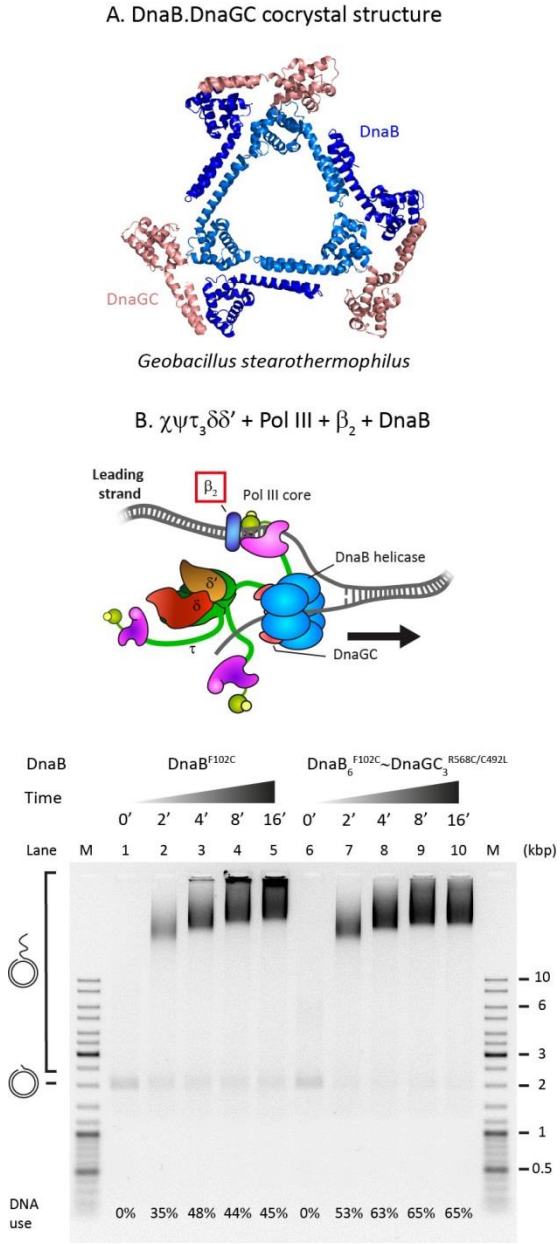

Figure 6.S5: $DnaB_6$.$DnaGC_3$ complex and its effect on leading-strand replication

Related to ***Figure 6.5***. (A) Cocrystal structure of $DnaB_6$.$DnaGC_3$ complex from *Geobacillus stearothermophilus* (Bailey et al., 2007) shows that three DnaGC molecules bind the DnaB hexamer (only the N-terminal domains of DnaB are displayed). (B) Top panel: cartoon presentation of the replisome components required to duplicate the leading strand (leading-strand synthesis). Unlike the replisomes used in leading-strand DNA synthesis assays shown in ***Figures 6.4***

and 6.5, the β_2 clamp is present in the current assay. Bottom panel: agarose gel shows DNA products obtained from leading-strand replication as a function of time (0, 2, 4, 8, and 16 min) with either $DnaB^{F102C}$ (lanes 1–5) or cross-linked $DnaB_6^{F102C}$~$DnaGC_3^{R568C/C492L}$ (DnaB~DnaGC; lanes 6–10).

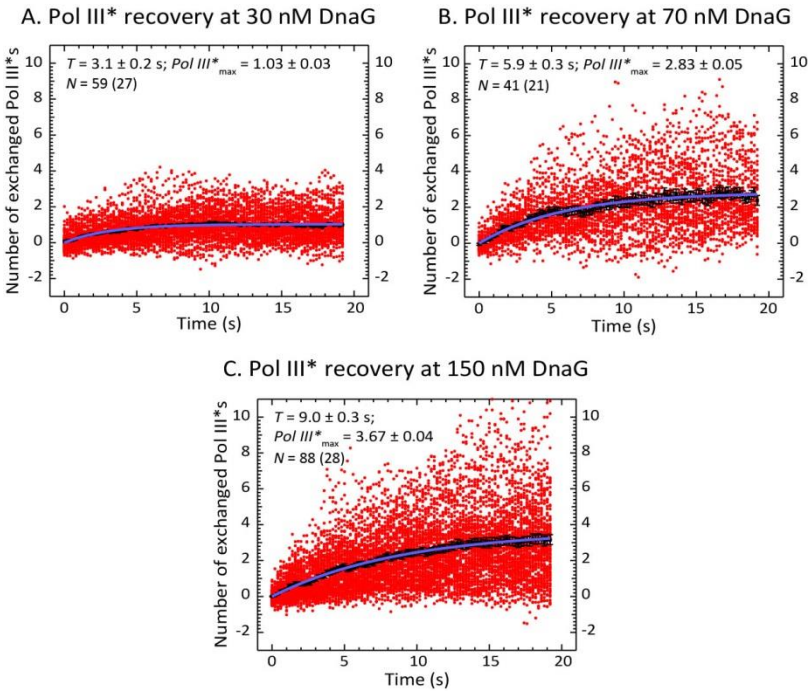

Figure 6.S6: Recoveries of fluorescence intensities following photobleaching at different DnaG concentrations

Related to ***Figure 6.6***. The indicated *N* number of intensities (red circles) obtained from the recovery intervals of a number of replisomes (displayed in brackets) at 30 (A), 70 (B) and 150 nM DnaG (C) are converted into the number of exchanged Pol III* and displayed, together with their average values (black squares). Fitting the evolution of average recovery intensities in time with FRAP recovery function (***Equation 6.3***) provided the characteristic (exchange) time (*T*) and the maximum number of exchanged Pol III* (*Pol III**$_{max}$), following the subtraction of fit background intensity y_0 that was previously converted into the number of Pol III*: (A) $T = 3.1 \pm 0.2$ s, *Pol III**$_{max}$ $= 1.03 \pm 0.03$, $y_0 = 0.42 \pm 0.03$; (B) $T = 5.9 \pm 0.3$ s, *Pol III**$_{max} = 2.83 \pm 0.05$, $y_0 = 0.20 \pm 0.05$; and (C) $T = 9.0 \pm 0.3$ s, *Pol III**$_{max} = 3.67 \pm 0.04$, $y_0 = 0.20 \pm 0.03$.